THERMODYNAMIC CYCLE SIMULATION OF A LARGE BORE, SINGLE CYLINDER, 2-STROKE NATURAL GAS ENGINE FOR PREDICTING EMISSIONS OF OXIDES OF NITROGEN

A Thesis

by

KEVIN LA MAR WALLACE

Submitted to the Office of Graduate and Professional Studies of
Texas A&M University
in partial fulfillment of the requirements for the degree of

MASTER OF SCIENCE

Chair of Committee,	Timothy J. Jacobs
Committee Members,	Jerald A. Caton
	Jorge L. Alvarado
Head of Department,	Andreas A. Polycarpou

August 2020

Major Subject: Mechanical Engineering

ABSTRACT

This work seeks to improve the current ability to model NO_x emissions from integral compressor engines that are commonly used in the natural gas industry. This improved understanding will be able to inform the development of future control technologies as the natural gas industry seeks to meet increasingly stringent emissions standards. To this end, a zero-dimensional thermodynamic cycle simulation was developed to predict NO_x emissions for a large bore, single cylinder, naturally aspirated, 2-stroke, natural gas engine. Excellent agreement was obtained between experimental measurements and simulated predictions of the average exhaust NO_x concentration.

Once the simulation was validated by experimental data, a sensitivity analysis was conducted to determine the response of NO_x emissions to changes in three factors: trapped equivalence ratio (TER), burned gas fraction (x_b), and stuffing box temperature (SBT). It was found that changes in each factor effected linear changes in the combustion temperatures, which effected linear changes in the rate constant of the first reaction in the extended Zeldovich mechanism, which effected exponential changes in the NO_x emissions. TER and SBT were shown to be directly related to NO_x, while x_b was shown to be inversely related to NO_x.

Finally, it was demonstrated that since NO_x is non-linearly related to in-cylinder pressure, an average cycle in terms of pressure is not necessarily an average cycle in terms of NO_x emissions. This fact underlines a need for future NO_x modeling efforts to account for cycle-to-cycle variations in engine behavior.

DEDICATION

To my parents, who have lovingly sacrificed so much for me.

ACKNOWLEDGEMENTS

I am indebted to so many individuals who have greatly enriched my experience as a student at Texas A&M. First, there is a genuine camaraderie among colleagues at the AERL, and I have been truly blessed to have an edifying and intellectually stimulating work environment among friends. Special thanks are in order for Abdullah Bajwa, Taylor Linker, and Forrest Pommier, who helped me collect all the experimental data for this work and greatly sharpened my understanding of many aspects of IC engines.

I would like to thank Dr. Jerald Caton for always making himself available to help me with my simulation. Without his assistance, I am doubtful that I ever could have completed this work. His helpful input and quality writings on thermodynamic simulations opened to me a rich and exciting research field. His mentorship has been a true blessing.

I am extremely thankful to Dr. Timothy Jacobs for accepting me into his research group and for supporting me in every way. He has always shown confidence in me, encouraged me in my work, and provided numerous opportunities for my professional growth. He was immediately my favorite professor when I took his class as an undergraduate student, and he has only grown in my estimation.

Words cannot express the gratitude and love I feel for my family. My parents, in particular, have sacrificed so much for my education and I absolutely never could have achieved my educational goals without their unconditional, unflagging love and support.

Of all the wonderful blessings I have received since coming to Texas A&M, none have been quite so sweet as my wonderful wife, Betsy. She has been my biggest fan and,

more than anyone else, has contributed to my great happiness in this season of life. I am so thankful for her friendship and help in all of my endeavors.

Finally, I must acknowledge my gratitude to God for blessing me so much more than I deserve with a wonderful family and an enjoyable experience at Texas A&M. This thesis seems to me somewhat of an Ebenezer stone; it is a tangible reminder that "thus far the Lord has helped [me]." I am also very grateful to have the opportunity to study thermodynamics, a fascinating part of His creation. It has allowed me more deeply to echo the ancient sentiment, "O the depth of the riches both of the wisdom and knowledge of God!"

CONTRIBUTORS AND FUNDING SOURCES

Contributors

This work was supervised by a thesis committee consisting of Professor Timothy Jacobs (advisor) and Professor Jerald Caton of the Department of Mechanical Engineering and Professor Jorge Alvarado of the Department of Manufacturing and Mechanical Engineering Technology.

The experimental data collected for this work was obtained with the assistance of Mr. Abdullah Bajwa, Mr. Taylor Linker, and Mr. Forrest Pommier. All other work conducted for the thesis was completed by the student independently.

Funding Sources

Funding for this work was graciously provided by Cooper Machinery Services. Its contents are solely the responsibility of the author and do not necessarily represent the official views of Cooper Machinery Services.

NOMENCLATURE

A	Area
a	Crank Radius
BDC	Bottom Dead Center
B	Cylinder Bore
C_p	Specific Heat at Constant Pressure
C_v	Specific Heat at Constant Volume
CAD	Crank Angle Degree
CO	Carbon Monoxide
CO_2	Carbon Dioxide
COV	Coefficient of Variation
CLD	Chemiluminescence Detection
E	Energy
EGR	Exhaust Gas Recirculation
EPC	Exhaust Ports Close
EPO	Exhaust Ports Open
γ	Ratio of Specific Heats $\left(\frac{C_p}{C_v}\right)$
h	Enthalpy
h_c	Convective Heat Transfer Coefficient
htm	Heat Transfer Multiplier
H	Monatomic Hydrogen

H_2	Diatomic Hydrogen
H_2O	Water
HAP	Hazardous Air Pollutants
HC	Hydrocarbons
IC	Internal Combustion
IMEP	Indicated Mean Effective Pressure
IPC	Intake Ports Close
IPO	Intake Ports Open
k^+	Forward Rate Constant
k^-	Reverse Rate Constant
ℓ	Length of Connecting Arm
m	Mass
N	Monatomic Nitrogen
N_2	Diatomic Nitrogen
N_2O	Nitrous Oxide
NO	Nitric Oxide
NO_2	Nitrogen dioxide
NO_x	Oxides of Nitrogen, NO and NO_2
O	Monatomic Oxygen
O_2	Diatomic Oxygen
OH	Hydroxide
P	Pressure

Q	Heat Transfer
R	Specific Gas Constant
RICE	Reciprocating Internal Combustion Engine
RPM	Revolutions Per Minute
SBT	Stuffing Box Temperature
t	Time
TDC	Top Dead Center
TER	Trapped Equivalence Ratio
T_{AF}	Adiabatic Flame Temperature
T_{EPC}	Temperature at exhaust port close timing
T_{SOC}	Temperature at the start of combustion
T_{wall}	Wall Temperature
u	Internal Energy
V	Volume
V_c	Clearance Volume
V_d	Displacement Volume
V_p	Mean Piston Speed
VOC	Volatile Organic Compound
W	Boundary Work
x_i	Mole (or Mass) fraction of species i
ϕ	Equivalence Ratio
θ	Crank Angle Degree

TABLE OF CONTENTS

Page

LIST OF FIGURES

Page

LIST OF TABLES

Page

1. INTRODUCTION

1.1. Motivation

Natural gas pipelines form a vital part of the energy infrastructure of the United States. In the contiguous 48 states, there are roughly 305,000 miles of transmission pipelines that supply much of the country's power and heating needs [1]. In order to move the natural gas through the pipelines to its desired destination, a network of over 1,400 compressor stations are used to provide pressure to the gas. Figure 1, taken from the Energy Information Administration, shows a map of the dense web of pipelines and compressor stations throughout most of the inhabited portions of the United States.

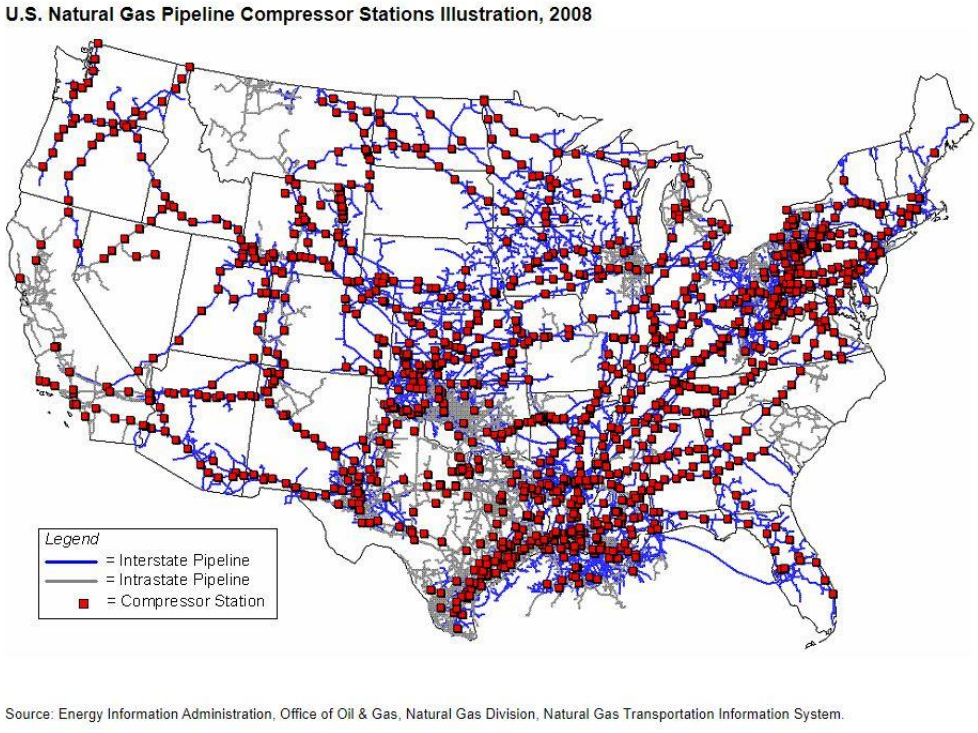

Figure 1: Map of Pipelines and Compressor Stations in the Lower 48 States as of 2008. Reprinted from [1].

The compressor stations utilize a variety of compressors, but the most efficient and cost-effective means of compressing the gas is through the use of an integral compressor engine, which is a reciprocating internal combustion engine (RICE) that is integrated with a compressor, i.e., the engine and the compressor share a common crankshaft [2]. Most of these integral compressor engines have been running for several decades and they still constitute a large portion of the compressor fleet.

Natural gas companies have massive financial incentives for maintaining the use of these engines as prime movers, not only because they are the most efficient means of compressing the natural gas, but also because the cost of halting their operation and installing new electric motors or cleaner engines as prime movers would be extremely expensive. So much so, that recent reports from the Pipeline Research Council International (PRCI) and the Interstate Natural Gas Association of America (INGAA) Foundation have expressed a willingness to spend millions of dollars in order to retrofit existing engines with new technology to keep them operating rather than to incur the financial hit of replacing them [2] [3] [4].

The reports from PRCI and INGAA reveal that although the existing fleet of integral compressor engines is very old, it is very robust and most of the engines could be operational for decades to come. Even so, due to increasingly stringent emissions regulations, pipeline companies face a serious challenge in continuing to operate these engines. Since most of the engines were designed before harmful air pollution began to be earnestly regulated, exhaust emissions were not a primary design consideration. Until now, however, most of these “legacy” engines have been grandfathered in newer

emissions regulations, allowing them to continue operating even though they do not meet current standards.

Air pollution legislation and regulation are very complicated, and the particular standard that an engine has to meet will depend on where it is located, its power output, when it was installed, and a variety of other factors [5]. Another complicating factor is that the standards are ever changing; it is impossible to predict the regulative climate moving forward, so pipeline companies can only guess the future emissions standards to which they will have to comply. However, the steady trend over the last 4 decades has been that air pollution regulation has become more and more stringent [6]. This steady trend has concerned pipeline companies that the grandfathered status of integral compressor engines may soon come to an end [2] [3].

The emissions most relevant to natural gas integral compressor engines are oxides of nitrogen (NO_x), volatile organic compounds (VOCs), and hazardous air pollutants (HAPs) [2] [3] [5]. The most notable VOCs are unburned hydrocarbons (HC) and formaldehyde. Formaldehyde is also the most notable HAP. Of these three classes of pollutants, the one that poses the biggest threat to the continuing operation of integral compressor engines is NO_x [3]. This work addresses the pressing need in the natural gas pipeline industry to reduce NO_x production from integral compressor engines.

1.2. Background

This section covers essential background information regarding the type of engine that is most common in the pipeline industry (2-stroke cycle engine) [3], the nature of NO_x pollution and its regulative history, and a broad overview of engine modeling. The sections

on 2-stroke cycle engines and NO_x pollution provide a technical and economic context for the problem addressed by this work, and the section on engine modeling explains why the simulation approach of this work was selected out of the pool of options available.

1.2.1. 2-Stroke Cycle Engines

Internal combustion (IC) engines are an important class of devices that convert chemical energy to mechanical energy. There have been a great variety of IC engine designs since the first IC engines became marketable in the early 1860s [7]. The 2-stroke cycle engine is one such type of IC engine, in which the combustion of a gaseous mixture of fuel and oxidizer (usually air) occurs in a reciprocating piston-cylinder device that drives a rotating shaft. Thus, chemical energy stored in the bonds of the fuel and oxidizer is converted to useful mechanical work. Figure 2 shows a schematic of a typical 2-stroke engine configuration. The 2-stroke cycle engine has a long history of providing power in a wide variety of applications, from lawn mowers and chainsaws to large locomotives and marine vessels [8] [9].

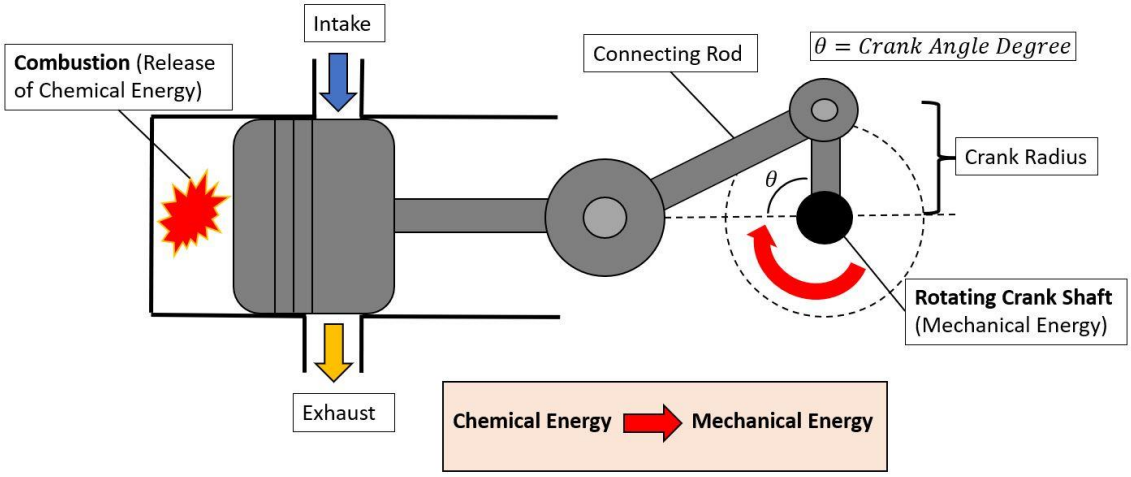

Figure 2: Schematic of a 2-Stroke Cycle Engine Converting Chemical Energy to Useful Mechanical Work

The name "2-stroke cycle" comes from the fact that these engines produce mechanical power by repeating the same process (or cycle) every 2 strokes of the piston. One complete thermodynamic cycle thus involves a full revolution of the crankshaft, or 360 crank angle degrees (CAD), as shown in Figure 2. The speed of the engine is usually given in terms of the number of revolutions of the crankshaft per minute, or RPM.

There are a variety of ways that a 2-stroke cycle engine can accomplish the task of completing a power cycle in one revolution of the crankshaft. The engines of interest for this work are a particular class of 2-stroke cycle engines that are direct injected and spark ignited. This means that the fuel induction to the cylinder is accomplished by injecting the fuel directly into the cylinder, and the combustion process is initiated by the electrical discharge of a sparkplug. Figure 3 shows the various stages of a 2-stroke cycle for such an engine.

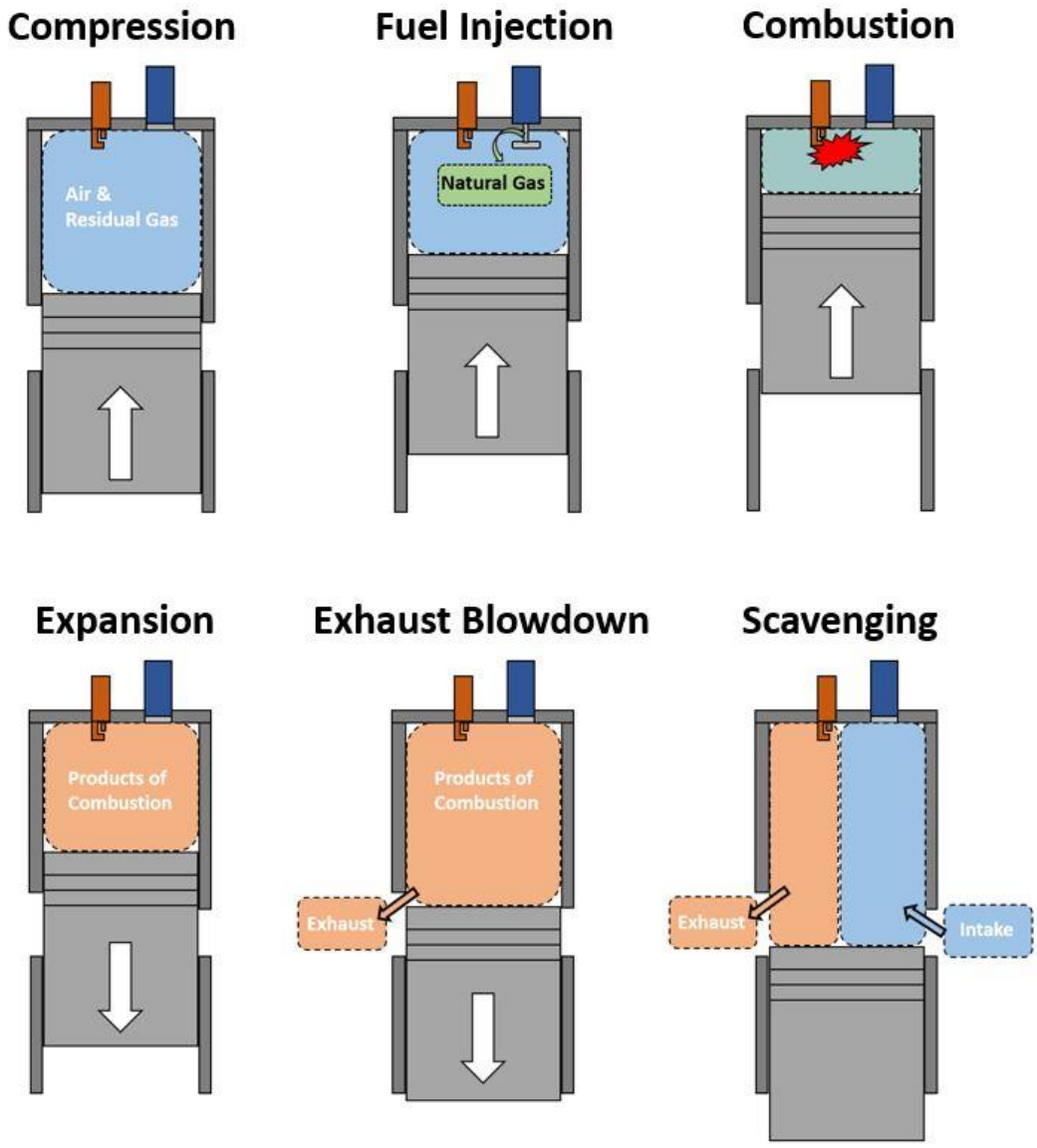

Figure 3: Stages of a 2-Stroke Cycle. Adapted from [10].

First, the piston compresses the newly inducted fresh air. Since the process of removing exhaust is not perfect, there are some burned combustion products that remain in the cylinder as residuals from the previous cycle. The ratio of burned residual gases to the total mass trapped in the cylinder is called the residual fraction (x_r). If there is no

exhaust gas recirculation (EGR), then x_r will equal the burned gas fraction (x_b), which is the ratio of burned gases to the total trapped mass prior to combustion.

Next, fuel is injected directly into the cylinder. This process can actually start earlier than compression because it is desirable to have the fuel as homogeneously mixed with the air as possible before combustion begins. This need for homogeneity is balanced by the desire to inject the fuel late enough so as not to let fuel escape with the exhaust without ever participating in combustion. This undesirable phenomenon is known as "short-circuiting" of the fuel, and it has been one of the chief drawbacks of 2-stroke engines as compared to their 4-stroke cousins. Since 4-stroke engines have two extra strokes per power cycle, they can easily isolate the fuel injection and exhaust processes.

Shortly before the piston reaches top dead center (TDC), the location in the cycle where the volume in the cylinder is at its minimum, the spark plug discharges an electric arc that initiates the combustion reaction. The hot gases will expand and push the piston forcefully back toward bottom dead center (BDC), the location in the cycle where the volume is at its maximum. After all the gas has combusted, the gas will continue to expand the piston until it reaches the opening of the exhaust port (EPO). This process of post-combustion expansion is often simply referred to as "expansion".

The exhaust ports open before the intake ports, i.e., EPO timing is before IPO timing. In this window between EPO and IPO, the exhaust blowdown occurs, where high energy combustion products are exhausted at high velocity, often at the speed of sound. After IPO, the exhaust and intake ports are both open, at which time the cylinder is simultaneously cleaned of burned gas and recharged with fresh gas. This combination of

intake and exhaust processes is referred to as "scavenging" [7]. There are multiple designs for scavenging a 2-stroke engine. These are normally lumped into three categories: cross-scavenged, loop-scavenged, and uniflow-scavenged configurations [7] [8]. Figure 3 depicts a cross-scavenged engine, where the intake and exhaust ports are on opposite sides of the cylinder. The engine examined in this work is also a cross-scavenged engine.

The intake air can be compressed by a turbocharger or supercharger before it enters the cylinder. The higher density of the compressed air means that more mass can be delivered to the cylinder. If the air is inducted without any turbocharging or supercharging, the engine is said to be "naturally aspirated." When the intake ports close (IPC), the exhaust port will again be open for a short time until it closes at EPC. EPC marks the end of one cycle, and a new cycle begins again by compressing the mixture of air and residual gases.

1.2.2. NO_x Pollution

Nitrogen oxides have been among the most significant air pollutants affecting the United States and other parts of the world. The following sections discuss two relevant aspects of the problem of NO_x pollution. First, the deleterious effects on human health and the integrity of the environment are together discussed as the "pollution problem." Second, there are important regulatory trends in the United States that have serious economic implications for industries burning fossil fuels. The regulatory trends affecting pipeline engine operators are discussed as the "economic problem."

1.2.2.1. The Pollution Problem

There are seven oxides of nitrogen known to science: NO, NO_2, NO_3, N_2O, N_2O_3, N_2O_4, and N_2O_5. Even though the label of "NO_x" can be used to designate all seven oxides of nitrogen, it is typically used to refer only to nitric oxide (NO) and nitrogen dioxide (NO_2) [6]. This is because NO and NO_2 are emitted in much greater amounts than the others due to their formation during the combustion of fossil fuels with air. Excess concentrations of NO_x in the atmosphere have been linked to a variety of harmful consequences for human health and the environment.

The link between NO_x emissions and urban smog was first discovered in the early 1950s by researchers studying the particularly egregious brown haze in Los Angeles [11]. The chemicals causing this objectionable phenomenon were found to be linked to photochemical reactions occurring between NO_x and VOCs. Later, the brown color was linked to NO_x molecules absorbing and scattering light in the visible spectrum [12]. The brown haze of smog can seriously impair visibility.

Important air pollution references list a litany of additional grim effects associated with excess NO_x concentrations and exposure to smog that have since been discovered, such as pulmonary fibrosis, emphysema, lower respiratory tract illness, and acid rain [6] [13]. These negative consequences of NO_x and other pollutants sparked a strong regulatory response from the federal government starting around the middle of the 20th century. This air pollution regulatory effort has continued and forms the basis for the economic problem of NO_x pollution.

1.2.2.2. The Economic Problem

Cooper and Alley provide a very helpful summary of the legislative and regulatory trends regarding air pollution in the United States [6]. This discussion borrows heavily from their work, highlighting the issues concerning NO_x emissions that are relevant to this work.

The first legal action against air pollution in the U.S. is traced back to the late 1800s, when certain large, industrial cities passed smoke control ordinances. As the problem of pollution increased, state and local governments devoted greater attention to its abatement. It was not until the middle of the 1900s, however, that the federal government first entered the arena of air pollution legislation through the passing of the Air Pollution Control Act of 1955. This act did not provide any means of enforcing air pollution standards, but it was the first step by the federal government to combat the problem.

The watershed moment for air pollution legislation in the United States came with the Clean Air Act Amendments of 1970. This established the Environmental Protection Agency (EPA), the National Ambient Air Quality Standards (NAAQS), and procedures that states had to follow in order to demonstrate compliance with federal standards. The NAAQS identified 6 criteria pollutants of chief concern, of which NO_x was one. States had to ensure that the concentration of these criteria pollutants met the requirements given by the NAAQS. Since 1970, the federal government has steadily increased its regulatory influence over the emission of air pollution by increasing the powers of the EPA and imposing stricter requirements for the NAAQS.

Most of the integral compressor engines in operation today, although they do not meet the current emissions standards for new sources given by the New Source Performance Standards (NSPS) [14], are still allowed to operate because they have been grandfathered in newer laws. Nevertheless, a report from the INGAA Foundation in 2014 revealed that industry experts expect new regulations in the next decade to threaten the continued operation of integral compressor engines [2]. The report outlines three reasons that will most likely trigger a need for increased NO_x control.

First, most new NO_x regulations for legacy engines arise from concerns over nonattainment of the ozone NAAQS, since NO_x is an important precursor to ground level ozone formation. Different states are expected to implement reasonably available control technology (RACT) rules in the coming years that will force existing pollution sources to adopt control strategies for NO_x abatement. Since the RACT rules assume that the necessary control technology is "reasonably available," even older legacy engines will have to comply with them. Indeed, several states, notably in the eastern U.S., have already passed RACT rules affecting integral compressor engines in those states.

Second, it is possible that the EPA will adopt a regional rule that specifies a certain NO_x reduction that is required for large sources. This would be a sweeping rule that would affect all of the states in a given region of the country. The INGAA report intimates that while possible, such a sweeping mandate is an unlikely course of action for the EPA.

Finally, a computer simulation technique called dispersion modeling has recently shown that emissions from certain compressor stations can travel off-site and bring other downwind areas into nonattainment of NO_x NAAQS requirements. Dispersion modeling

is commonly used by the EPA for calculating the movement of pollution emitted from smoke stacks by following the dispersion of the smoke plume. This has not posed a major problem for pipeline companies yet, but the threat of legal action for off-site pollution could occur at any time.

The above discussion illustrates the "economic problem" facing pipeline companies today. Pipeline companies would like to continue operating legacy integral compressor engines, but increasingly stringent emissions regulations threaten their continued operation. In order to continue legally operating these engines, pipeline companies need to implement new control strategies. The current research is important in addressing this problem because a deep understanding of the fundamental thermodynamic processes of an engine is crucial to the development of a control strategy. It is difficult to control that which is not understood.

1.2.3. Engine Cycle Simulation

Thermodynamic analysis of combustion engines has a rich history dating back to the late 19th century [15]. Although the earliest attempts at modeling thermodynamic cycles achieved modest successes, the models remained highly simplistic until the advent of computers. Since the 1960s, computer simulations have greatly expanded upon the thermodynamic insights of primitive models [16].

The first computer models in the 1960s (e.g., [17] [18]) were zero-dimensional thermodynamic models, i.e., the bulk thermodynamic properties of the cylinder gases were calculated throughout the cycle without spatial resolution. In other words, the thermodynamic properties of the cylinder gases were calculated as a function of time, but

not as a function of space. These types of simulations experienced a flurry of development throughout the 1970s and 1980s [7].

As engine research progressed and as computer hardware improved, multi-dimensional simulations started to become commonplace. These simulations are usually three-dimensional computational fluid dynamics programs that are often capable of staggeringly sophisticated calculations. Although these simulations are certainly more capable than their zero-dimensional counterparts at capturing the complicated physical processes occurring in an engine, they are orders of magnitude more computationally expensive. For this reason, zero-dimensional models are still widely used today, because even though they are less detailed, their ability to provide rapid results makes them amenable to real-time control applications and parametric sensitivity analyses [16].

A zero-dimensional thermodynamic cycle simulation was selected for the current work in order to complete a parametric sensitivity analysis, identifying certain fundamental thermodynamic factors affecting NO_x formation in an engine and quantifying their respective effects. It is also hoped that the current computer simulation will continue to be developed to allow for real time engine control of NO_x emissions.

2. LITERATURE REVIEW

This section presents a literature review of zero-dimensional thermodynamic cycle simulation of IC engines and its use to calculate NO_x emissions.

2.1. General Principles

A vast body of literature exists for zero-dimensional cycle simulation and a complete summary of the subject is well beyond the scope of this work. This literature review focuses on those aspects of the subject that are most relevant to the current work. The reader will note that extensive use is made of Caton's publications [16] [19]. The cycle simulation developed for the current work is heavily indebted to his previous contributions.

Zero-dimensional thermodynamic cycle simulations treat the contents of an engine cylinder (i.e., the cylinder gases) as a thermodynamic control system that obeys the first law of thermodynamics and the ideal gas equation of state. As will be shown in this section, judicious use of the first law of thermodynamics and the ideal gas equation of state, along with a set of simplifying assumptions, allows the thermodynamic properties of the cylinder gases to be calculated throughout an engine cycle (360 CAD for a 2-stroke cycle engine).

It is important to emphasize that in the following sections, derivatives with respect to time (t) can also be seen as derivatives with respect to CAD (θ). If the engine speed (RPM) is known, then a derivative with respect to time can be converted to a derivative with respect to CAD, and vice versa.

This first section (2.1) of the literature review describes the main aspects of these types of simulations. Later sections (2.2 - 2.4) of the literature review focus in greater depth upon portions of the simulation that require more detailed consideration.

2.1.1. Assumptions

The set of simplifying assumptions used in developing these types of simulations can vary somewhat depending on the type of engine analyzed, the experimental data available as inputs to the model, and the type of resulting information that is desired. The following list, adapted from Caton [16] [19], reveals a set of assumptions that is typical for zero-dimensional thermodynamic cycle simulations.

1) The thermodynamic system is the cylinder contents.
2) The engine is in steady-state such that the thermodynamic state at the beginning of each cycle is equivalent to the state at the end of the cycle.
3) For compression and expansion processes, the cylinder contents are spatially homogeneous and occupy one zone.
4) The gas exchange portion of an engine cycle is very different for 2-stroke and 4-stroke engines. This is an especially challenging process to model in 2-stroke engines, and more information on the set of assumptions needed for this item is presented in section 2.3.
5) For the combustion process, the cylinder gases can be assumed to consist of either one, two, or three zones, where each zone is spatially homogeneous.
6) The thermodynamic properties (including pressure and temperature) vary only with time (crank angle) and are spatially uniform in each zone.

7) The instantaneous composition is obtained from generally accepted algorithms and the species obey the ideal gas equation of state [7] [20].
8) The instantaneous thermodynamic properties are computed from established formulations based on the appropriate compositions [7].
9) The flow rates into and out of the system are determined from quasi-steady, one-dimensional flow equations.
10) The fraction of fuel burned in the engine is specified by a Wiebe function, where the combustion efficiency is nearly 100% (i.e., no unburnt fuel).
11) Blow-by is neglected, i.e., there is no mass flow into the crevices between the piston and the cylinder wall.

These assumptions will be of varying validity depending upon the particular engine that is being modeled, but they have each been widely and successfully used for many years and for many types of engines [21] [22] [23].

2.1.2. Thermodynamic Formulations

This section describes how the first law of thermodynamics is used along with the above assumptions to obtain the equations needed to calculate the thermodynamic properties throughout the engine cycle. This section will only consider a one-zone gas mixture, where at any given CAD, the entirety of the cylinder gases are assumed to be at the same thermodynamic state.

The goal of this step is to obtain an equation for the derivatives of thermodynamic properties from which the thermodynamic state at the subsequent time step can be approximated. For an ideal gas of fixed composition, two independent thermodynamic

properties are needed to fully define the thermodynamic state [24]. For this reason, the first law of thermodynamics is typically used with the ideal gas equation of state to obtain derivatives for either temperature, pressure, or density [7] [25]. Once derivatives for two of these three properties have been obtained, the third property can easily be calculated from the ideal gas law.

The first law of thermodynamics states that energy is conserved [24]. When this principle is applied to a control system, it entails that the rate of change of the energy inside the control system is equal to the rate at which energy is entering the system minus the rate at which energy is leaving the system. This sentence is given a mathematical description in equation (1) below.

$$\dot{E}_{system} = \dot{E}_{in} - \dot{E}_{out} \tag{1}$$

In thermodynamics, there are three possible energy interactions at the boundary of a control system: heat transfer, work, and mass transfer [24]. Figure 4 below illustrates the energy flows in an IC engine.

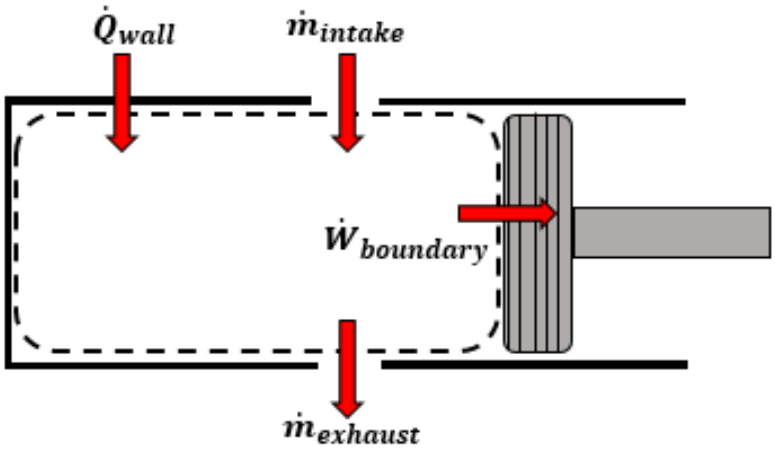

Figure 4: Energy Accounting for an IC Engine

The application of the first law of thermodynamics to the above control system leads to the following equation, where u is internal energy, h is enthalpy, m is mass, Q is heat transfer (assumed positive into the system), and W is boundary work (assumed positive out of the system).

$$\left(\frac{dE}{dt}\right)_{system} = \frac{d(mu)}{dt} = \dot{m}u + m\dot{u} = \dot{Q} - \dot{W} + \dot{m}_{in}h_{in} - \dot{m}_{out}h_{out} \qquad (2)$$

The heat transfer, internal energy, enthalpy, and mass flow rate terms are calculated using methods explained in later sections. The boundary work is calculated as the product of the gas pressure and the volume derivative, as shown in equation (3) below.

$$\dot{W} = P\dot{V} \qquad (3)$$

Generally, the internal energy of an ideal gas mixture of known composition can be assumed to vary only with temperature [26]. This is true in an engine as well. However, at the high temperatures encountered during combustion and expansion, there can often be dissociation and recombination reactions that change the composition of the gas [24].

Thus, in order to calculate the internal energy of the high temperature combustion gases, a method is needed to calculate temperature and gas composition.

The dissociation and recombination reactions are typically modeled by assuming the gas mixture is in chemical equilibrium [7]. The equilibrium calculations, described in section 2.1.5, are dependent upon the gas pressure and the reactant composition, i.e., the equivalence ratio (ϕ) [20].

The internal energy can therefore be assumed to be a function of temperature, pressure, and reactant composition. The time derivative of internal energy can then be calculated using the chain rule, as seen in equation (4).

$$\dot{u} = \frac{\partial u}{\partial T}\dot{T} + \frac{\partial u}{\partial P}\dot{P} + \frac{\partial u}{\partial \phi}\dot{\phi} \tag{4}$$

At lower temperatures, the gas composition can be assumed to be fixed, or "frozen," and thus the $\dot{P}$ and $\dot{\phi}$ terms can be dropped. The cutoff temperature at which this "frozen" assumption can be made varies from author to author. For example, Heywood cites 1700 K as a good cutoff [7], while Caton recommends 1200 K for best accuracy [16]. This approach to calculating the internal energy has become well-established [7] [16] [25].

As a reminder, the goal of this section is to obtain equations for the time derivatives of two independent thermodynamic properties. Thus far, the first law of thermodynamics has been used to obtain an equation that contains the time derivatives of temperature and pressure. An additional equation is now needed in order to solve explicitly for $\dot{T}$ and $\dot{P}$.

This additional equation can be obtained by taking the derivative of temperature or pressure with respect to time in the ideal gas equation, and doing the necessary algebra

to solve for the derivatives of temperature and pressure explicitly. Caton gives the following final results of this process [19], shown in equations (5) - (12) below (where R is the specific gas constant of the one-zone mixture).

$$\dot{T} = \frac{G(1 + P_1)}{mC_v(1 + P_2)} \tag{5}$$

$$\dot{P} = \frac{mR\dot{T} + m\dot{R}T + \dot{m}RT}{V} \tag{6}$$

where,

$$G = \dot{Q} - P\dot{V} + \dot{m}_{in}h_{in} - \dot{m}_{in}h_{in} - u\dot{m} \tag{7}$$

$$P_1 = \frac{\alpha_1}{G} \tag{8}$$

$$P_2 = \frac{\alpha_2}{C_v} \tag{9}$$

$$\alpha_1 = m\left\{\frac{\partial u}{\partial \phi}\dot{\phi} + \frac{\frac{\partial u}{\partial P}}{V\beta}\left(-mT\frac{\partial R}{\partial \phi}\dot{\phi} - \dot{m}RT + P\dot{V}\right)\right\} \tag{10}$$

$$\alpha_2 = \frac{\frac{\partial u}{\partial P}}{\beta}P\left(\frac{1}{T} + \frac{1}{R} + \frac{\partial R}{\partial T}\right) \tag{11}$$

$$\beta = 1 - \frac{P}{R}\frac{\partial R}{\partial P} \tag{12}$$

These equations are very general, and in most cases many of the terms can be neglected. For instance, during the compression process, the system is closed and the composition of the gas is assumed to be fixed. Therefore, there are no derivatives of the mass, gas constant, or equivalence ratio. This greatly simplifies the above expressions.

With these expressions for $\dot{T}$ and $\dot{P}$, the temperature and pressure at the next time step can be calculated using a finite difference approximation. For a gas of known composition, the thermodynamic state is fully defined when the temperature and pressure are specified. However, in order to use these expressions to calculate the thermodynamic state, methods are needed to specify the gas composition and the various terms in the above equations (such as $\dot{Q}$ and the partial derivatives of thermodynamic properties). The specification of these items is addressed next in the following sections (2.1.3. - 2.1.8.).

2.1.3. Kinematic Equations

In order to solve the equations that were derived using the first law of thermodynamics and the ideal gas equation of state, the cylinder volume and its time derivative need to be specified at every point in the engine cycle. Thus, an expression for each term is needed as a function of CAD. A variety of kinematic relationships have been developed for such a purpose based on the geometry of the engine [7] [25]. The following kinematics relationships, given by equations (13) and (14), are taken from Caton [16]. The terms in these relationships are illustrated in Figure 5.

$$V(\theta) = V_c + \frac{\pi B^2}{4}(\ell + a - s) \tag{13}$$

$$\dot{V}(\theta) = \frac{dV}{d\theta} = \frac{\pi B^2}{4} a\sin(\theta)\left[1 + \frac{a\cos(\theta)}{[\ell^2 - a^2\sin^2(\theta)]^{\frac{1}{2}}}\right] \tag{14}$$

where,

$$s = a\cos(\theta) + [\ell^2 - a^2\sin^2(\theta)]^{\frac{1}{2}} \tag{15}$$

$$V_c = Clearance\ Volume\ (i.e., Volume\ at\ TDC)$$

$$\ell = Length\ of\ Connecting\ Rod$$

$$a = Crank\ Radius$$

$$B = Cylinder\ Bore$$

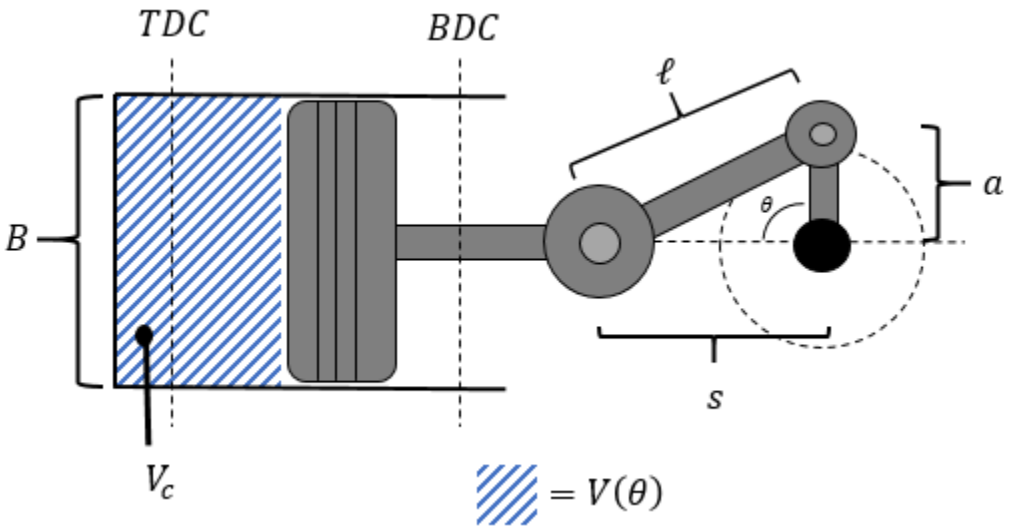

Figure 5: Schematic of Cylinder Geometry for Kinematic Relations

In addition to the cylinder volume and its time derivative, it is also usually desirable to calculate the surface area of the cylinder as a function of CAD because of its use in heat transfer sub-models. Caton provides a relationship for this as well [16] using the geometric parameters listed above. This relationship is given in equation (16).

$$A(\theta) = A_{top} + A_{bottom} + A_{side} = \frac{\pi B^2}{2} + \pi B(\ell + a - s) \qquad (16)$$

2.1.4. Determination of Mixture Composition

The calculation of the unburned and burned mixture composition can proceed in many different ways depending upon the engine that is being simulated and the experimental data available. In any case, it is necessary to have an algorithm that is capable

of calculating the mole fractions of the reactants (unburned mixture) and the products (burned mixture) of the combustion reaction. The composition of the gas is needed in order to fully define the thermodynamic state.

A classic algorithm for this purpose is given by Heywood [7], and is described in this section. Since this work is interested in fuel-lean ($\phi < 1$) integral compressor engines, the presentation of the algorithm in this section is limited to fuel-lean operation. This algorithm uses ϕ and x_b as inputs. Thus, in order to use this algorithm, ϕ and x_b must be calculated either from experimental measurements or from simulated estimates.

The algorithm assumes that the reactants are a general hydrocarbon fuel $(CH_y)_\alpha$, air, and some residual products of combustion. It assumes that the products are merely carbon dioxide (CO_2), water (H_2O), excess oxygen (O_2), and nitrogen (N_2). In other words, it assumes complete combustion of the hydrocarbon fuel. Using this algorithm, the mole fractions can be calculated as follows:

Step 1: Calculate/Specify Necessary Parameters

a) $\phi = Specified\ by\ User$

b) $x_b = Specified\ by\ User$

c) $\alpha = Specified\ by\ User$

d) $y = Specified\ by\ User$

e) $\psi = Ratio\ of\ \frac{N_2}{O_2}\ in\ air = 3.773$

f) $M_f = Molecular\ Weight\ of\ Fuel = \alpha(12 + y)$

g) $\varepsilon = \frac{4}{4+y}$

Step 2: Calculate Unburned Mole Fractions

a) $n_b = (1-\varepsilon)\phi + 1 + \psi$

b) $n_u = (1-x_b)\left[\frac{4(1+2\varepsilon)\phi}{M_f} + 1 + \psi\right] + x_b n_b$

c) $n_f = \frac{4(1-x_b)(1+2\varepsilon)\phi}{M_f}$

d) $n_{CO2,u} = x_b \varepsilon \phi$

e) $n_{H2O,u} = 2x_b(1-\varepsilon)\phi$

f) $n_{O2,u} = 1 - x_b\phi$

g) $n_{N2,u} = \psi$

h) $x_{f,u} = mole\ fraction\ of\ fuel\ (unburned) = \frac{n_f}{n_u}$

i) $x_{CO2,u} = mole\ fraction\ of\ CO_2\ (unburned) = \frac{n_{CO2,u}}{n_u}$

j) $x_{H2O,u} = mole\ fraction\ of\ H_2O\ (unburned) = \frac{n_{H2O,u}}{n_u}$

k) $x_{O2,u} = mole\ fraction\ of\ O_2\ (unburned) = \frac{n_{O2,u}}{n_u}$

l) $x_{N2,u} = mole\ fraction\ of\ N_2\ (unburned) = \frac{n_{N2,u}}{n_u}$

Step 3: Calculate Burned Mole Fractions

a) $n_{CO2,b} = \varepsilon\phi$

b) $n_{H2O,b} = 2(1-\varepsilon)\phi$

c) $n_{O2,b} = 1 - \phi$

d) $n_{N2,b} = \psi$

e) $x_{CO2,b} = mole\ fraction\ of\ CO_2\ (burned) = \frac{n_{CO2,b}}{n_b}$

f) $x_{H2O,b} = mole\ fraction\ of\ H_2O\ (burned) = \frac{n_{H2O,b}}{n_b}$

g) $x_{O2,b} = mole\ fraction\ of\ O_2\ (burned) = \frac{n_{O2,b}}{n_b}$

h) $x_{N2,b} = mole\ fraction\ of\ N_2\ (burned) = \frac{n_{N2,b}}{n_b}$

The above three steps in the algorithm allow the user to calculate the mole fractions (i.e., the composition) of the unburned and burned mixtures. However, as mentioned earlier, when the temperatures are very high during combustion and expansion, the products can dissociate into smaller molecules. This dissociation can have a significant impact on the calculation of internal energy and enthalpy. Also, as mentioned earlier, at these high temperatures it is customary to model the combustion products as being in chemical equilibrium. The following section (2.1.5.) describes how to calculate the equilibrium composition of the combustion products.

2.1.5. Calculation of Equilibrium Concentrations of Combustion Products

There are many different product species that can result from combustion. The state-of-the-art chemical mechanism for modeling natural gas combustion, the GRI-Mech 3.0, contains 325 reactions and 53 different gas species [27]. If desired, the equilibrium concentrations of all 53 species could be calculated by minimizing the Gibbs and Helmholtz free energies for a given reacting mixture at a given temperature and pressure. Computer programs of this sort have been developed since the 1960s [28].

However, since these programs are computationally expensive and the vast majority of possible product species exist in miniscule amounts in normal IC engine operation, it is typical to only consider roughly 10-15 product species in the equilibrium

calculations [29]. A classic computer program by Olikara and Borman [20], considering 12 product species, has been of particular utility for modeling IC engines because it not only calculates the equilibrium mole fractions, but it also calculates the partial derivatives of those mole fractions with respect to temperature, pressure, and equivalence ratio. These partial derivatives can be used to calculate the partial derivatives of the internal energy, enthalpy, and the specific gas constant of the product gases.

The method of Olikara and Borman considers a combustion reaction of the following form (where x_{13} is defined such that the chemical reaction produces 1 mole of products):

$$x_{13}\left[C_nH_nO_\ell N_k + \frac{n+\frac{m}{2}-\frac{\ell}{2}}{\phi}(O_2 + \psi N_2 + \xi Ar)\right] \rightarrow x_1H + x_2O + x_3N + x_4H_2 + x_5OH + x_6CO + x_7NO + x_8O_2 + x_9H_2O + x_{10}CO_2 + x_{11}N_2 + x_{12}Ar \quad (17)$$

Olikara and Borman use $\psi = 3.7274$ and $\xi = 0.0444$. In order to stay consistent with Heywood's algorithm for determining the unburned and burned compositions, Caton uses $\psi = 3.773$ and $\xi = 0$ [16]. The current work follows Caton.

There are thirteen unknown molar coefficients in equation (17). Thus, thirteen independent equations are needed to solve for them all. Five equations can be obtained from atom balances of each element in the reaction. An additional equation is obtained by noting that all of the molar coefficients on the right-hand side sum to 1. The remaining 7 equations are obtained from the following equilibrium reactions.

$$\frac{1}{2}H_2 \rightleftarrows H \quad (18)$$

$$\frac{1}{2}O_2 \rightleftarrows O \tag{19}$$

$$\frac{1}{2}N_2 \rightleftarrows N \tag{20}$$

$$\frac{1}{2}H_2 + \frac{1}{2}O_2 \rightleftarrows OH \tag{21}$$

$$\frac{1}{2}N_2 + \frac{1}{2}O_2 \rightleftarrows NO \tag{22}$$

$$H_2 + \frac{1}{2}O_2 \rightleftarrows H_2O \tag{23}$$

$$CO + \frac{1}{2}O_2 \rightleftarrows CO_2 \tag{24}$$

The equilibrium constant for each of the above reactions can be calculated based on curve-fits to the JANAF thermochemical tables [30]. Olikara and Borman detail a solution procedure using the Newton-Raphson iterative technique. Since this method calculates the equilibrium mole fractions as a function of temperature, pressure, and equivalence ratio, the partial derivatives of the mole fractions can also be calculated with respect to temperature, pressure, and equivalence ratio.

2.1.6. Calculation of Thermodynamic Properties

The thermodynamic properties of an ideal gas mixture can be calculated as the weighted sum (on a molar or mass basis) of the properties of its individual constituents [24], as seen in equation (25), where β is any thermodynamic property of interest. This equation is often used in thermodynamic cycle simulation to calculate the specific heats, internal energy, and enthalpy of the gas mixture.

$$\beta_{mix} = \sum x_i \beta_i \tag{25}$$

Curve fits for the specific heat at constant pressure (C_p) and enthalpy as functions of temperature are available from several sources (e.g., [27]) for a wide range of gases. These curve fits are generally polynomials of the following form:

$$\frac{C_p}{R} = a_1 + a_2 T + a_3 T^2 + a_4 T^3 + a_5 T^4 \tag{26}$$

$$\frac{h}{RT} = a_1 + \frac{a_2 T}{2} + \frac{a_3 T^2}{3} + \frac{a_4 T^3}{4} + \frac{a_5 T^4}{5} + \frac{a_6}{T} \tag{27}$$

For an ideal gas, the specific heat at constant volume (C_v) and the internal energy can be obtained from the following relationships:

$$C_v = C_p - R \tag{28}$$

$$u = h - RT \tag{29}$$

Using these polynomials to calculate u, h, C_v, and C_p as functions of temperature, and using Olikara and Borman's method to calculate the equilibrium mole fractions and their partial derivatives with respect to temperature, pressure, and equivalence ratio, the partial derivatives of u and h with respect to temperature, pressure, and equivalence ratio can be calculated. This is a complicated process, but it is described in detail by Olikara and Borman [20].

2.1.7. Calculation of Heat Transfer

The heat transfer between the cylinder walls and the cylinder gases is a very complex process that must be grossly simplified for zero-dimensional models. The heat transfer has both a convective and radiative component, but the radiative component is generally negligible for SI engines [7]. The convective heat transfer from the walls to the cylinder gases is given by the following equation, taken from Caton [16]:

$$\dot{Q} = h_c A(\theta)(T_{wall} - T) \tag{30}$$

where h_c is the instantaneous convective heat transfer coefficient and T_{wall} is the cylinder wall temperature.

Several correlations have been proposed for h_c in the past. The correlation provided by Woschni, based on an analysis of data from diesel engines, has been among the most popular and widely used [31]. The final form of Woschni's correlation, adjusted to be presented in units of $\left[\frac{W}{m^2 \cdot K}\right]$, is given by Caton [16] in equation (31) below.

$$h_c\left[\frac{W}{m^2 \cdot K}\right] = 3.26(B[m])^{-0.2}(P[kPa])^{0.8}\left(w\left[\frac{m}{s}\right]\right)^{0.8}(T[K])^{-0.55} \tag{31}$$

where, V_p is the mean piston speed, V_d is the displacement volume, P_m is the motoring pressure at that CAD, and P_r, T_r, and V_r are the pressure, temperature, and volume, respectively, at some reference point in the cycle. The w term is a characteristic velocity term given by the following equation:

$$w = C_1 V_p + C_2 \frac{V_d T_r}{P_r V_r}(P - P_m) \tag{32}$$

$$For\ the\ Gas\ Exchange\ Period: C_1 = 6.18;\ C_2 = 0 \tag{33}$$

$$For\ the\ Compression\ Period: C_1 = 2.28;\ C_2 = 0 \tag{34}$$

$$For\ the\ Combustion\ Period: C_1 = 2.28;\ C_2 = 0.00324 \tag{35}$$

Sometimes, in order to tune the heat transfer model to experimental data, a heat transfer multiplier (htm) is applied to the heat transfer calculation. The calculation of cylinder heat transfer is very difficult for zero-dimensional models. Due to this difficulty, rather than calculating the heat transfer from fundamental principles of thermodynamics,

the heat transfer sub-model often acts as a tuning knob that allows the simulation to more closely match the experimental data.

2.1.8. Calculation of the Thermodynamic State at a Subsequent Time-Step

Once the derivatives of the thermodynamic properties have been solved, they can be used to calculate the thermodynamic state at a subsequent time-step using a finite difference approximation. As an example, upon calculating $\dot{T}$ and $\dot{P}$ at time i, a first-order finite difference approximation for T and P at time $i+1$ for a given time-step Δt is given below.

$$T_{i+1} = T_i + \dot{T}_i \Delta t \tag{36}$$

$$P_{i+1} = P_i + \dot{P}_i \Delta t \tag{37}$$

Using the methods presented in sections 2.1.4. and 2.1.5 to specify the mixture composition, the thermodynamic state at $i+1$ can be fully defined by calculating T_{i+1} and P_{i+1} according to equations (36) and (37).

2.2. Combustion Modeling

Although the thermodynamic formulations for a one-zone gas mixture were presented in section 2.1. in such a way as to permit the modeling of combustion, it is very common to use a multi-zone model in order to capture more thermodynamic details [19] [22]. For instance, significant thermodynamic gradients can exist between the unburned and burned gases to which one-zone models are blind [21].

Two-zone models are the most common type of multi-zone model, but other multi-zone models have been formulated for specific purposes as well [22]. This section presents an overview of two-zone combustion modeling and a description of a three-zone modeling

technique first developed by Heywood et al. [21] for the purpose of calculating NO_x emissions.

2.2.1. Two-Zone Combustion Model

Two-zone models are based upon the physical phenomenon in spark-ignition engines that a flame front of burning gas propagates through the unburned gas during the combustion process. The two-zone model divides the cylinder contents into two separate control systems, separated by an infinitesimally thin flame front [16] [22], over which mass from the unburned zone moves into the burned zone throughout the combustion process, as depicted in Figure 6.

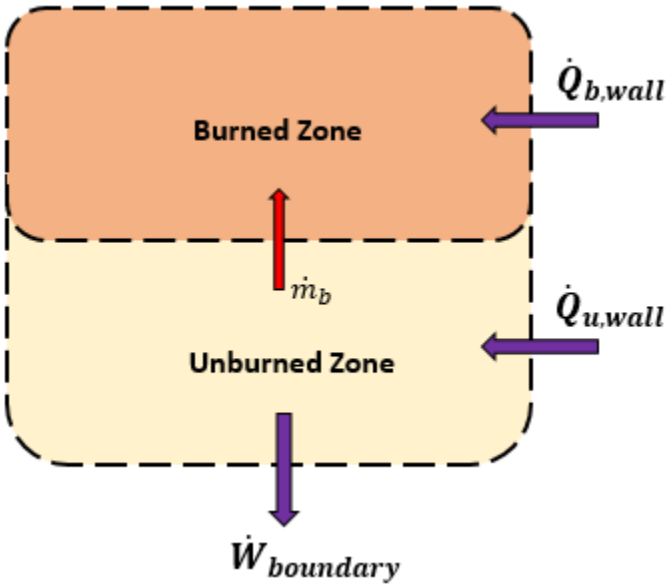

Figure 6: Schematic of a Two-Zone Combustion Model

The first law of thermodynamics can be applied to both the unburned and burned control systems, and each control system is assumed to obey the ideal gas equation of state. In this way, two equations for each zone can be formulated for the derivatives of

their respective thermodynamic properties. These four equations, together with the continuity equation, lead to a system of five ordinary differential equations that can be solved for the derivatives needed to approximate the thermodynamic state of each zone at the subsequent time-step. A detailed derivation of this process is provided by Caton [16], and his resulting system of differential equations is provided below.

$$\dot{T}_b = \frac{\dot{Q}_b - P\dot{V}_b + \dot{m}_b(h_u - u_b) - m_b\frac{\partial u_b}{\partial P}\dot{P} - m_b\frac{\partial u_b}{\partial \phi}\dot{\phi}}{m_b C_{v,b}} \tag{38}$$

$$\dot{T}_u = \frac{\dot{Q}_u - P\dot{V}_u + \dot{m}_u R_u T_u}{m_u C_{v,u}} \tag{39}$$

$$\dot{P} = \frac{m_b R_b \dot{T}_b + m_b T_b\left(\frac{\partial R_b}{\partial T_b}\dot{T}_b + \frac{\partial R_b}{\partial \phi}\dot{\phi}\right) + \dot{m}_b(T_b R_b - T_u R_u) + m_u R_u \dot{T}_u - P\dot{V}}{V\left(1 - \frac{m_b\frac{\partial R_b}{\partial P}T_b}{V}\right)} \tag{40}$$

$$\dot{V}_u = V_u\left(\frac{\dot{m}_u}{m_u} + \frac{\dot{T}_u}{T_u} - \frac{\dot{P}}{P}\right) \tag{41}$$

$$\dot{V}_b = \dot{V} - \dot{V}_u \tag{42}$$

In addition to the information already provided in section 2.1. for a one-zone formulation, in order to solve equations (38) - (42), methods are needed to specify the rate at which mass enters the burned zone and the proportion of the total heat transfer that is attributed to each zone.

Several methods are available for prescribing the rate at which mass moves from the unburned zone to the burned zone. The fraction of mass burned in the cylinder as a function of crank-angle has been very simply modeled by a portion of a cosine function

(e.g., [32]). More sophisticated models have tried to predict the burning rate based upon experimentally derived correlations for the growth of the flame front (e.g., [33]).

One of the most well-known and widely used methods is to prescribe the mass fraction burned curve with a Wiebe function [7] [16]. Since the Wiebe function is an analytical expression, the derivative of the mass fraction burned curve can also be calculated. The mass fraction burned curve and its derivative, using a Wiebe function, are provided in the following equations:

$$x_b\left[\frac{mass\ burned}{total\ mass}\right] = 1 - \exp\left(-a\left(\frac{\theta - \theta_o}{\theta_b}\right)^{m+1}\right) \tag{43}$$

$$\dot{x}_b\left[\frac{mass\ burned/_{total\ mass}}{radians}\right] = \frac{a(m+1)}{\theta_b}\left(\frac{\theta - \theta_o}{\theta_b}\right)^{m} \exp\left(-a\left(\frac{\theta - \theta_o}{\theta_b}\right)^{m+1}\right) \tag{44}$$

where a and m are parameters that can be tuned to match experimental data, θ is the instantaneous CAD, θ_o is the CAD at the start of combustion, and θ_b is the burn duration in CAD. The form of these equations is taken from Caton [16].

The total heat transfer is usually calculated according to a correlation such as the Woschni correlation provided in section 2.1.7. This total heat transfer is usually allocated between the two zones by assuming that the fraction of the total cylinder surface area covered by each zone is proportional to each zone's respective volume fraction [16] [22]. Furthermore, since the two zones are at different temperatures, the heat transfer calculation should be in proportion to their temperatures. Caton provides one such possible scheme for allocating the total heat transfer between the zones [16]. This scheme is given by equations (45) and (46).

$$\dot{Q}_u = \left(\frac{V_u}{V_{total}}\right)^{\frac{2}{3}} \left(\frac{T_{wall} - T_u}{T_{wall} - T}\right) \dot{Q}_{total} \tag{45}$$

$$\dot{Q}_b = \dot{Q}_{total} - \dot{Q}_u \tag{46}$$

2.2.2. Three-Zone Combustion Model

The two-zone model is sufficient for calculating the bulk thermodynamics inside the engine. However, a more detailed model is needed in order to calculate NO_x formation in the engine. As will be described in section 2.4., the chemical kinetics of NO formation are extremely sensitive to temperature. For this reason, and due to the fact that large temperature gradients can exist in the burned gases, the average temperature of the burned zone is an insufficient input for a NO_x sub-model.

In an effort to account for this thermal gradient, Heywood et al. [21] proposed a three-zone combustion model, where the burned zone is split into two zones: an adiabatic core zone and a boundary layer zone. This model is based on the notion that combustion takes place in a hot, adiabatic core, and as the flame front expands, previously burned gas forms a thin boundary layer around the adiabatic core. All of the heat transfer from the burned zone goes to the boundary layer zone. Figure 7 shows a schematic of this three-zone control system.

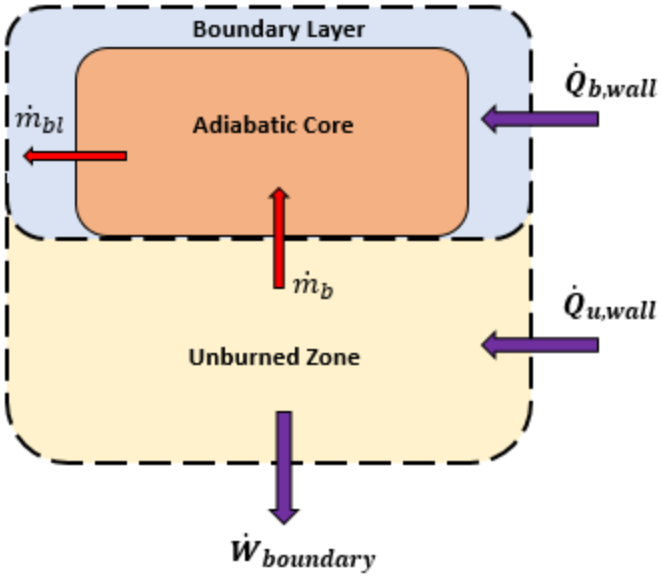

Figure 7: Schematic of a Three-Zone Combustion Model

Similar to the one-zone and two-zone formulations, the first law of thermodynamics, ideal gas equation of state, and the continuity equation can be applied to each of the three zones. With the additional assumption that the boundary layer temperature is equal to the logarithmic mean temperature of the adiabatic core temperature and the wall temperature, six more differential equations can be obtained that need to be solved in conjunction with the five differential equations derived from the two-zone formulation in order to calculate the thermodynamic states of each zone at the subsequent time-step. Caton provides the resulting six differential equations [16], reproduced below.

$$\dot{T}_a = \frac{-P\dot{V}_a + \dot{m}_b(h_u - u_a) - \dot{m}_{bl}R_aT_a - m_a\frac{\partial u_a}{\partial P}\dot{P} - m_a\frac{\partial u_a}{\partial \phi}\dot{\phi}}{m_a C_{v,a}} \tag{47}$$

$$\dot{T}_{bl} = \left[\frac{1}{\ln\left({}^{T_a}/_{T_{wall}}\right)} - \frac{1 - {}^{T_{wall}}/_{T_a}}{\left(\ln\left({}^{T_a}/_{T_{wall}}\right)\right)^2}\right]\dot{T}_a \tag{48}$$

$$\dot{V}_{bl} = V_{bl}\left(\frac{\dot{m}_{bl}}{m_{bl}} + \frac{\dot{R}_{bl}}{R_{bl}} + \frac{\dot{T}_{bl}}{T_{bl}} - \frac{\dot{P}}{P}\right) \tag{49}$$

$$\dot{V}_a = \dot{V}_b - \dot{V}_{bl} \tag{50}$$

$$\dot{m}_{bl} = \frac{\dot{Q}_b - P\dot{V}_{bl} - m_{bl}\left(C_{v,bl}\dot{T}_{bl} + \frac{\partial u_{bl}}{\partial P}\dot{P} + \frac{\partial u_{bl}}{\partial \phi}\dot{\phi}\right)}{u_{bl} - h_a} \tag{51}$$

$$\dot{m}_a = \dot{m}_b - \dot{m}_{bl} \tag{52}$$

2.3. Scavenging Modeling

One of the most difficult aspects of thermodynamic simulations of two-stroke cycle engines is modeling the scavenging process. Since the intake and exhaust valves/ports are open simultaneously for much of the gas exchange process, certain assumptions must be made in order to calculate the change in composition of the mixture. A variety of single and multi-zone models of varying complexity have been proposed [8] [9]. The two classic one-zone scavenging models are the "perfect displacement" and "perfect mixing" models [34].

The perfect displacement model is an idealization that as the incoming fresh mixture enters the cylinder, it pushes the burned gases out of the exhaust port, such that no incoming fresh mixture can pass through the exhaust port until all the burned gas has exited. The perfect mixing model is an idealization that as the incoming fresh mixture enters the cylinder, it instantly and completely mixes with the existing cylinder gases. Figure 8 shows a schematic of these two models.

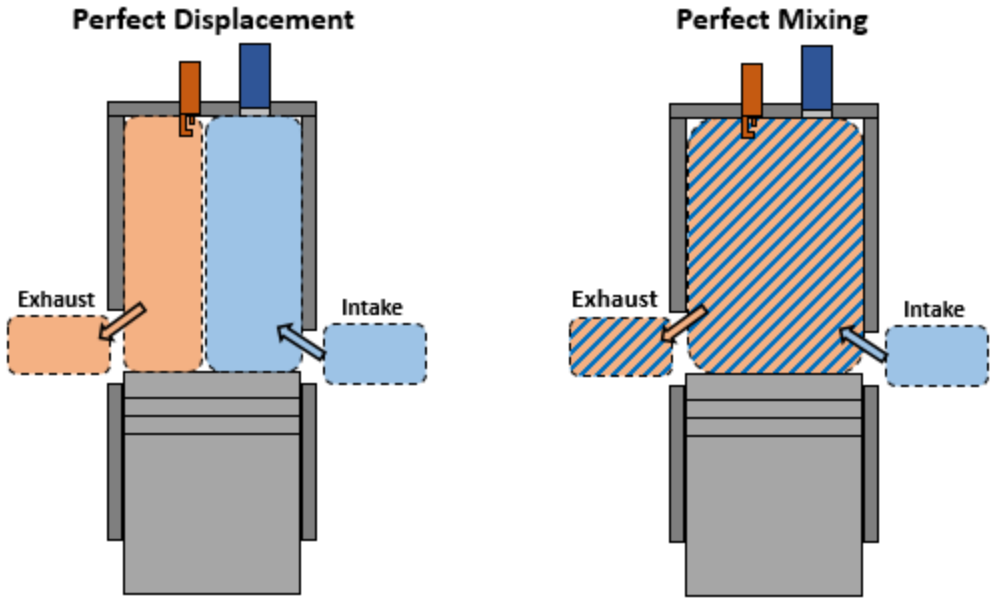

Figure 8: Schematic of the Perfect Displacement and Perfect Mixing Models

Every two-stroke engine exhibits different scavenging behavior, so the degree of accuracy of these two models varies from engine to engine. Typically, actual scavenging behavior is somewhere in between the predictions of these two models [8].

In general, when these two models have been used, the entirety of the scavenging process is modeled as occurring at constant volume [9] [34]. However, both the perfect displacement and perfect mixing assumptions can be used along with the one-zone thermodynamic formulation presented in section 2.1.2., in which the volume is not assumed constant.

In order to use either the perfect mixing or perfect displacement model, equations are needed to calculate the intake and exhaust mass flow rates. These equations can be obtained using the equation for one-dimensional, isentropic, compressible flow through a flow restriction [7]. The form of this equation is different depending on if the flow is

subsonic or sonic ("choked"). A version of these equations, taken from Caton [16], is reproduced below:

$$Subsonic: \dot{m} = A_t P_u \sqrt{\frac{2}{RT_u}\left(\frac{P_t}{P_u}\right)^{2/\gamma}\left(\frac{\gamma}{\gamma-1}\right)\left[1-\left(\frac{P_t}{P_u}\right)^{(\gamma-1/\gamma)}\right]} \tag{53}$$

$$Sonic: \dot{m} = A_t P_u \sqrt{\frac{\gamma}{RT_u}\left(\frac{2}{\gamma+1}\right)^{\gamma+1/\gamma-1}} \tag{54}$$

where, A_t is the cross-sectional area over which flow occurs, γ is the ratio of specific heats, P_u is the upstream pressure, P_t is the downstream pressure, and T_u is the upstream temperature. The flow will be sonic if the following inequality is satisfied:

$$\frac{P_u}{P_t} \geq \left(\frac{\gamma+1}{2}\right)^{\gamma/\gamma-1} \tag{55}$$

2.4. NO_x Prediction

Since NO_x has been recognized for many years as one of the most significant pollutants, many attempts have been made to model and predict its formation in an engine. One of the difficulties in modeling NO_x is that, unlike most of the other product species, it cannot be accurately modeled by assuming it has reached chemical equilibrium. The chemical kinetics of NO_x formation are such that the time scales at which NO and NO_2 reach chemical equilibrium are usually much longer than the time scales of engine speeds [7].

There are four primary chemical mechanisms responsible for NO_x formation in an engine: the thermal (or extended Zeldovich) mechanism, the prompt (or Fenimore) mechanism, the N_2O-intermediate mechanism, and the fuel nitrogen mechanism [16] [35].

Of these four, the extended Zeldovich mechanism is typically by far the most dominant mechanism, especially for spark ignition engines [7]. The Fenimore mechanism can be significant at rich conditions, and the N_2O-intermediate mechanism can become significant for very lean, low-temperature conditions [35]. For most spark-ignition engines, the fuel nitrogen mechanism is negligible [16].

Since the extended Zeldovich mechanism is usually dominant and is the mechanism used in the current work, the remainder of this section will focus on its use to calculate NO_x formation. All of the NO_x formed by the Zeldovich mechanism is NO.

There are three reactions in the extended Zeldovich mechanism:

$$O + N_2 \rightleftarrows NO + N \tag{56}$$

$$N + O_2 \rightleftarrows NO + O \tag{57}$$

$$N + OH \rightleftarrows NO + H \tag{58}$$

From chemical kinetics, the derivative of the NO concentration can be given as a function of the concentrations of each molecule in the chemical mechanism as follows:

$$\frac{d[NO]}{dt} = k_1^+[O][N_2] + k_2^+[N][O_2] + k_3^+[N][OH] - k_1^-[NO][N] - k_2^-[NO][O] - k_3^-[NO][H] \tag{59}$$

where k_1^+, k_2^+, and k_3^+ are the forward rate constants of the first, second, and third reactions in the extended Zeldovich mechanism, respectively; k_1^-, k_2^-, and k_3^- are the reverse rate constants of the first, second, and third reactions in the extended Zeldovich mechanism, respectively; and the bracketed values are the concentrations of each molecule in

dimensions of moles per volume. The rate constants are experimentally obtained and published as functions of temperature (e.g., [7] [36]).

Often times, equation (59) can be put in a form that is more amenable to calculation by assuming that the concentrations of O, N_2, O_2, OH, and H are in equilibrium, and that N is in steady-state (i.e., its time derivative is zero) [16] [35]. After making these assumptions, a simpler expression for the derivative of the NO concentration can be obtained. Equation (60) is a clean form of this expression, taken from Caton [16].

$$\frac{d[NO]}{dt} = \frac{2R_1(1-\beta^2)}{1+\beta K} \tag{60}$$

where,

$$R_1 = k_1^+[O][N_2] \tag{61}$$

$$R_2 = k_2^+[N][O_2] \tag{62}$$

$$R_3 = k_3^+[N][OH] \tag{63}$$

$$\beta = \frac{[NO]_a}{[NO]_e} \tag{64}$$

$$K = \frac{R_1}{R_2 + R_3} \tag{65}$$

In equation (64), the $[NO]_e$ term refers to the equilibrium NO concentration, which can be calculated using the method of Olikara and Borman that was described earlier. The $[NO]_a$ term refers to the actual NO concentration, which should be updated each time-step.

It should be emphasized that equation (60) is the derivative of the NO concentration at a given volume, in dimensions of moles per volume. It is not the total

derivative of the NO concentration because the volume of the engine cylinder is changing. Therefore, in using equation (60), the amount (in moles or mass) of NO formed or removed should be calculated after each time-step.

3. METHODS

3.1. Experimental Technique

3.1.1. Engine Description and Specifications

The engine used for this study was an Ajax E-565. This is a naturally aspirated, 2-stroke, single cylinder, natural gas engine, commonly used to power pump jacks in oil fields. The relatively small size, but similar design of this engine compared to those that are normally used in the pipeline industry is attractive for research purposes because experimental work is much more manageable for smaller engines. Figure 9 shows the Ajax, fully instrumented, in the Advanced Engine Research Laboratory at Texas A&M. The specifications for the Ajax are given in Table 1 [37] [38].

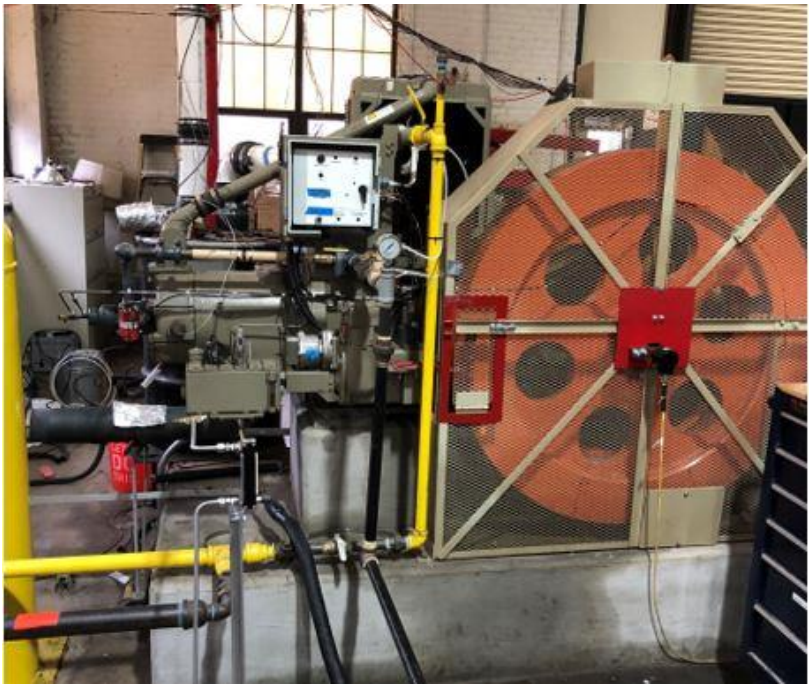

Figure 9: The Ajax E-565 in the Advanced Engine Research Laboratory at Texas A&M

Table 1: Ajax E-565 Engine Specifications (Rated for Ambient Temperature of 100°F)

Rated Continuous Brake Horsepower	40 hp (29.8 kW)
Rated Engine Speed	525 RPM
Torque	400 ft-lb (542 N-m)
BMEP	53.6 psi (370 kPa)
Displacement Volume	9.29 L
Bore	8.5 in. (216 mm)
Stroke	10 in. (254 mm)
Effective Compression Ratio	6:1

In order to mitigate the problems caused by short-circuiting, most integral compressor engines are retrofitted with direct injection systems. Although not a typical feature of the Ajax E-565, a direct injection system was installed for this engine as well, allowing the Ajax to mimic the behavior of the majority of the integral compressor engine fleet.

Gas chromatograph measurements taken by the utility company show that the composition of the natural gas fuel is around 95% methane, 2% ethane, and the remaining 3% consists of N_2, CO_2, and heavier hydrocarbons. It is important to state that the cycle simulation assumed that the entirety of the fuel was methane. This was done to simplify the combustion chemistry and the calculation of various thermodynamic properties, but the presence of other gas species in the fuel could warrant further attention in future work.

3.1.2. Instrumentation Utilized and Data Collected

Experimental data was collected primarily for two purposes. First, zero-dimensional models require experimental inputs to tune the simulation. Second,

experimental data is needed to validate the simulation results. The following discussion will identify first the experimental data used as inputs to the simulation, and second, the experimental data needed to validate the simulation.

The fuel flow rate was measured using an Alicat low pressure drop mass flow meter (MW-1000SLPM-D), capable of measuring 0-1000 SLPM. A low pressure drop meter was needed because the natural gas entering the building was already at the relatively low pressure of around 12 psi. The Alicat flow meter allows the fuel to reach the injector at a pressure of 8-10 psi, depending on the speed of the engine and the ambient temperature. The fuel flow meter was connected to the data acquisition system so that time averaged measurements could be made. The time averaged fuel flow rate was used to specify the average amount of fuel mass introduced each cycle.

The stuffing box and exhaust pipe pressures were measured using a Kistler piezoresistive pressure transducer. These time-resolved pressure measurements, recorded every fourth of a CAD, were used to calculate the intake and exhaust mass flow rates during the gas exchange process. The stuffing box temperature was measured using a K-type thermocouple. This datum was used to prescribe the temperature of the intake air in the simulation.

A rotary optical encoder made by Dynapar (HSD25 series) was used to record the revolution of the crankshaft with 0.25 CAD resolution (1440 PPR). This capability enabled the in-cylinder, stuffing box, and exhaust pipe pressures to all be measured as a function of CAD. This encoder was also able to log instantaneous and time averaged engine speed (RPM).

The in-cylinder pressures were measured using a Kistler piezoelectric pressure transducer. The pressure data during combustion was used to identify the Wiebe parameters for the combustion sub-model, and the data during gas exchange was used to tune the average intake and exhaust discharge coefficients. The pressure data was also used as a first step in validating the simulation, by comparing the simulated pressure curve to the experimental curve.

A Horiba MEXA-7100D emissions bench with a CLA-720MA NO/NO_x analyzer was used to measure the NO_x emissions [39]. The NO_x emissions were measured using the principle of chemiluminescence. The NO in the exhaust stream was mixed with ozone (O_3) in a high temperature reactor to form O_2 and nitrogen dioxide in an excited state, denoted as NO_2^*. As the NO_2^* relaxes to ground state NO_2, it emits light. This light is perceptible by a chemiluminescence detector (CLD), where the amount of light emitted is related to the amount of NO present. This process is illustrated in the following chemical reactions below [7] [39]:

$$NO + O_3 \rightarrow NO_2^* + O_2 \tag{66}$$

$$NO_2^* \rightarrow NO_2 + hv \tag{67}$$

Since the NO_2 that already exists in the exhaust stream cannot be excited by reacting with O_3 in this way, it must first pass through a converter, where all the NO_2 is reduced to NO, and then sent through the CLD. In this way, the analyzer measures the total NO_x concentration, but it does not distinguish between NO and NO_2.

The exhaust gas is dehumidified before it enters the analyzer, so all NO_x emissions are reported as dry measurements. The NO_x concentration in the exhaust was measured in parts per million (ppm).

Table 2 below summarizes the important experimental data collected.

Table 2: Summary of Experimental Measurements

Experimentally Measured Parameter	Measured Value
Engine Speed	520 RPM (99% of rated speed)
Torque	357 ft-lb (89% of full load)
Fuel Flow Rate	211 SLPM (0.27 g/cycle)
COV of IMEP	9%
Average Exhaust NO_x Concentration	169 ppm
Stuffing Box Temperature	314.5 K
In-Cylinder, Intake, and Exhaust Pressure	4 samples/CAD (1440 samples/cycle)

3.2. Simulation Framework

This section discusses the main components of the thermodynamic cycle simulation, with a particular emphasis on the NO_x prediction sub-model. Following this discussion, the methodology for a sensitivity analysis is described, where the simulation was used to computationally investigate the effects of TER, x_b, and SBT on the exhaust concentration of NO_x.

3.2.1. Thermodynamic Models

The simulation divided the two-stroke cycle into four sections, and each section had its own sub-model. The four main sub-models of the current simulation are compression, combustion, expansion, and gas exchange. Figure 10 shows the timing

diagram for when these sub-models are operative in the cycle. Each of these four processes will be described in order. The heat transfer model is operative throughout the engine cycle and will be discussed after the four main sub-models. Finally, the methods concerning how the initial conditions were marched in time to converge to a solution are described.

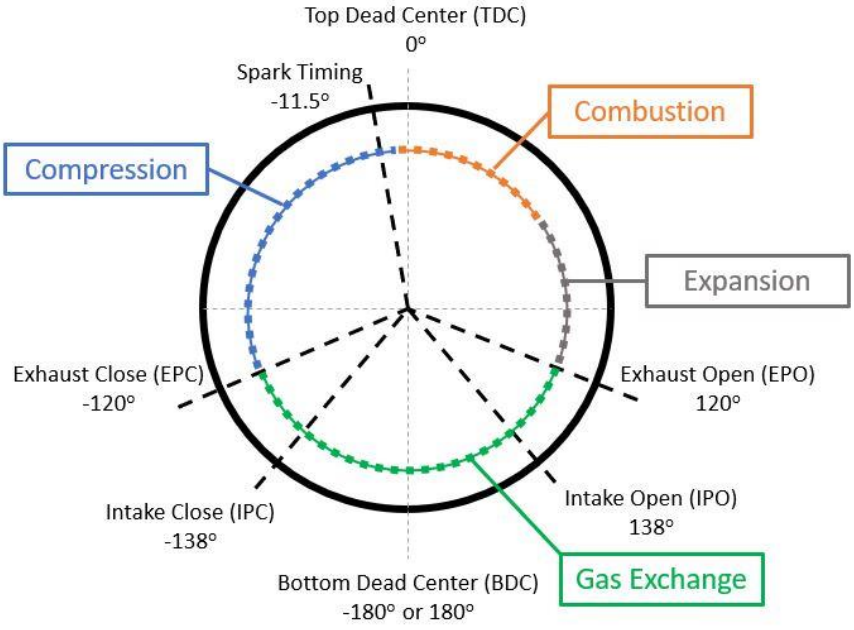

Figure 10: Timing Diagram for Ajax E-565 and the Cycle Simulation. Adapted from [38].

3.2.1.1. Compression

The compression process is the simplest of the four main sub-models. The gas during compression was modeled as a one-zone mixture. The initial temperature, pressure, and composition of the mixture are specified by the initial conditions. The process of specifying initial conditions is described later in 3.2.1.7. During compression, the composition of the mixture is assumed to be constant since there are no chemical reactions

such as combustion or dissociation occurring, and the system is closed, i.e., there is no transfer of mass across the boundaries of the thermodynamic system.

The one-zone model was chosen instead of a polytropic process model because it more rigorously accounts for the various thermodynamic processes occurring during compression. For instance, it tracks changing specific heats and heat transfer, whereas the polytropic process model simply selects an average ratio of specific heats that is tuned to match the experimental pressure curve.

3.2.1.2. Combustion

Since the aim of this work was to predict NO_x emissions, and since the NO formation is so sensitive to temperature, a combustion model was needed that would account for the variation of temperature in the cylinder. For this reason, a three-zone model was used for the combustion process.

A Wiebe function was used to prescribe the rate at which mass from the unburned zone is entrained in the adiabatic core. The Wiebe function was tuned by getting the simulated pressure curve to match the experimental pressure curve. Therefore, this is a non-predictive combustion model. The burn duration was chosen to be 56 CAD, and the a and m values in the Wiebe function (equation (43)) were chosen to be 5 and 1.81, respectively.

The equilibrium mole fractions of the combustion products, as well as the partial derivatives of their thermodynamic properties, were calculated at each time step using the method described by Olikara and Borman [20].

3.2.1.3. Expansion

The expansion process is very similar to the compression process, since each can be modeled as a one-zone gas in a closed thermodynamic system. However, the far higher temperatures existing in expansion result in two primary differences between the expansion and compression processes.

First, since the temperatures during expansion are quite high (~1600 – 2000 K), the cylinder gas is not assumed to be fixed in composition because dissociation and recombination reactions can occur. Instead, the equilibrium mole fractions of the gas are updated at each time step.

Second, the NO_x prediction sub-model is operative during the expansion process, so the adiabatic core and boundary layer zones continue to be tracked throughout the expansion process.

3.2.1.4. Gas Exchange

The gas exchange process involves mass transfer in three places: the exhaust ports, the intake ports, and the fuel injector. As the timing diagram in Figure 10 showed, the exhaust ports were open for the entirety of the gas exchange process, but the intake ports only participated in part of the gas exchange process. The author is in the unfortunate position of not knowing the exact timing of the opening and closing of the fuel injector valve, indeed there is probably cycle-to-cycle variability in the injection timing.

Several simulated trials showed, however, that the timing of fuel injection had little effect on the thermodynamics of the compression process, since the fuel only comprises roughly 3% of the total trapped mass. For a zero-dimensional simulation, since fluid

mechanics calculations are neglected and the trapped mass is assumed to be homogeneous, the important information regarding fuel injection is the total fuel mass trapped in the cylinder.

Since the majority of fuel is injected either late in the exhaust process or after the exhaust ports have closed, it was assumed that the duration of fuel injection lasted from IPC to EPC. This assumption allowed the compression process to be a totally closed system.

The perfect mixing model was used to model the scavenging process. This idealization most likely, but not necessarily, leads to a slight overprediction of x_b [8]. The perfect mixing assumption and the assumption for injection timing are both necessary simplifications for this zero-dimensional model, but they limit the ability to track the composition of the cylinder gas mixture with much detail.

The average discharge coefficients of the intake and exhaust ports were chosen to be 0.56 and 0.68, respectively.

3.2.1.5. Heat Transfer

The Woschni correlation was used to model heat transfer. A heat transfer multiplier (htm) of 1 was used for compression, combustion, and gas exchange, but an htm of 0.85 was used for the expansion process. The average wall temperature was chosen to be 400 K; this temperature was largely used as a tuning knob, but experimental data on an Ajax-2800, a similar engine to the Ajax E-565, showed that 400 K is within a reasonable range. When the Woschni correlation was used for the combustion and

expansion processes, the motoring pressure was estimated by a polytropic process. Heat transfer was calculated throughout the cycle.

3.2.1.6. NO_x Prediction Model

Since the thermal nitric oxide mechanism is known to be the cause of the vast majority of NO_x production in most cases [7] [16], all of the NO_x in the simulation is assumed to be formed through the thermal mechanism, i.e., the three chemical reactions in the extended Zeldovich mechanism. The rate constants for each reaction were taken from Dean and Bozzelli [36].

This work is merely concerned with the total NO_x emissions, so the simulation only calculates NO formation or destruction, but it does not predict any subsequent oxidation of NO to NO_2. Furthermore, for spark-ignition engines, the ratio of NO_2/NO is usually very small anyways [7].

The NO_x prediction model involves two main steps. First, NO formation is calculated throughout the combustion and expansion processes, resulting in a final NO concentration at the end of expansion. This concentration of NO in the burned gases is assumed to be fixed, or "frozen", for the entirety of the gas exchange process because the temperatures are too low for NO kinetics to be significant. Second, since the exhaust gas is diluted by short-circuited air, the exhaust concentration of NO will be lower than the NO concentration at the end of expansion. This effect of dilution must be accounted for in the simulation.

3.2.1.7. Initial Conditions and Convergence of the Simulation

To begin the simulation, the thermodynamic state of the cylinder gas was defined at EPC by guessing an initial pressure, temperature, TER, and x_b. From this point, the derivatives of the thermodynamic properties were calculated and a first order accurate, forward finite difference approximation was used to march the simulation in time.

The simulation starts at EPC with the compression process and proceeds until 1.25º before TDC. Once the compression process ends, the combustion process begins, and the final thermodynamic state of the compression process becomes the initial thermodynamic state of the combustion process. Even though the spark timing happens 11.5º before TDC, the effects of combustion were imperceptible until many crank angles later, so an ignition delay was given to the simulation and the combustion sub-model did not begin until 1º before TDC. The combustion model proceeded until 55º after TDC.

Once combustion ends, expansion begins, and once expansion ends, gas exchange begins. The final thermodynamic state at the end of one sub-model becomes the initial state for the next sub-model, as described in the above paragraph.

Once one complete cycle has been completed, the final thermodynamic state at the end of gas exchange is compared to the initial state at the beginning of compression. If these two states are similar to within an accepted tolerance, the simulation ends, but if the two states are sufficiently different, then the final state is prescribed as the initial state for the next cycle, and the simulation is run again. This process continues until the simulation converges. For this work, the simulation was assumed to converge once the final temperature was within ±0.0005 K of the initial temperature, the final pressure was within

±0.0005 kPa of the initial pressure, and the final TER and x_b were within ±5 x 10^{-9} of their initial values.

Table 3 displays the initial conditions to which the simulation converged, as well as the predicted exhaust concentration of NO for a cycle that has reached steady-state operation with those initial conditions. These values form what is henceforth referred to as the "base case," which served as a control group for the sensitivity analysis.

Table 3: Initial Thermodynamic State to Which the Simulation Converged

Parameter	Simulated Value	Parameter	Simulated Value
TER	0.7133	Exhaust [NO]	174 ppm
x_b	0.1488	Trapped Mass	7.8 g
T_{EPC}	457.2 K	P_{EPC}	117.3 kPa

3.3. Sensitivity Analysis

Due to the uncertainty attending various assumptions and experimental inputs upon which the current simulation relies, a concomitant uncertainty accompanies the NO_x prediction results. The following discussion highlights key areas of uncertainty in the simulation inputs, and then describes the sensitivity analysis that was conducted to investigate how the NO_x prediction responds to changes in these important inputs to the simulation.

Among the most important experimental data used in the simulation are the fuel flow rate, the engine speed, and the intake air temperature. The average fuel flow rate and engine speed are used together to calculate the average mass of fuel injected in the cylinder each cycle as follows:

$$mass\ of\ fuel\ injected\ \left[\frac{g}{cycle}\right] = \frac{Fuel\ Flow\ Rate\ \left[\frac{g}{min}\right]}{RPM\ \left[\frac{cycles}{min}\right]} \tag{68}$$

The average fuel mass injected each cycle is thus directly proportional to the fuel flow rate and inversely proportional to the engine speed.

The temperature of the intake air affects how much air mass is introduced each cycle. Higher temperature air has a lower density, so less fresh air mass is normally introduced for higher intake temperatures. The intake air temperature air also determines the enthalpy and specific heats of fresh gas entering the engine. The most important ramification of this fact is that higher temperature air coming into the cylinder will result in higher temperatures of the unburned gas mixture just before combustion. The flame temperature of the products of combustion depends on the temperature of the reactant mixture. So, in theory, higher intake air temperatures should result in higher burned gas temperatures.

Each of these experimental inputs affects the initial conditions of the simulation at EPC, namely the amount and composition of trapped mass, and the internal energy (or temperature) of the trapped mass.

In addition to these experimental inputs to the simulation, there are a few key assumptions that must be made in certain sub-models of the simulation. Perhaps the most tenuous of such in this simulation is the perfect-mixing assumption for the scavenging process. Although a simplifying assumption like perfect-mixing is necessary for zero-dimensional simulations, it renders impossible the detailed tracking of gas species

throughout scavenging. This inability can lead to errors in the simulation's initial conditions for the composition of the trapped mixture at EPC.

Based on the above discussion, the items chosen to vary in the sensitivity analysis were the trapped equivalence ratio (TER), the burned gas fraction (x_b), and the stuffing box temperature (SBT), because these three items are key initial conditions for the simulation that affect the amount, composition, and temperature of the trapped mass. The calculations for TER and x_b are influenced by the fuel flow rate, engine speed, and SBT measurements, and by the assumptions of the scavenging model used. The SBT measurement influences the calculations for the amount and temperature of air mass delivered to the cylinder.

The base case was taken to be the thermodynamic cycle simulation that was described in section 3.2, in which the simulated pressure trace matches an experimentally obtained average pressure trace. In the sensitivity analysis, the TER and x_b were each varied ±3%, 6%, and 9% from the base case values. The SBT was varied ±5 K, 10 K, and 15 K from the base case value. The exhaust NO_x concentration was calculated for each condition examined. Tables 4-7 in Appendix A provide a list of the conditions examined.

4. RESULTS AND DISCUSSION

4.1. NO_x Prediction

The first step in validating the thermodynamic cycle simulation was to compare the simulated pressure curve with experimental pressure data. Figure 11 below shows this comparison between crank-angle resolved pressure curves; one was calculated by the simulation and the other was obtained experimentally from an average of 1,460 consecutive cycles.

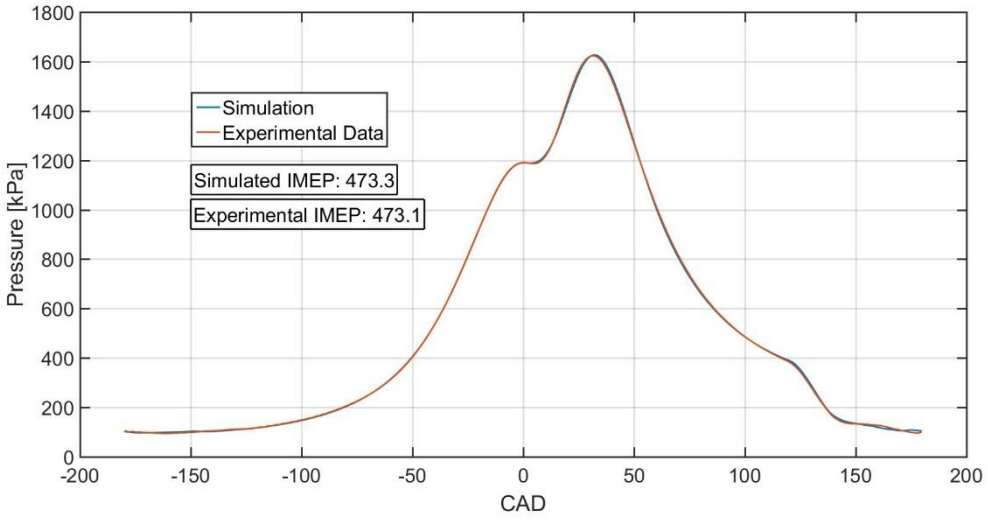

Figure 11: Comparison of Experimental and Simulated Pressure Curves for an Average Cycle

It should be stressed that this step involved some ad-hoc tuning of the sub-models in order to get the simulated pressure to match the experimental data this well. The primary tuning knobs were the discharge coefficients of the intake and exhaust ports, the heat transfer model (via the wall temperature and htm), and the Wiebe function.

The discharge coefficients were adjusted to achieve pressure matching during gas exchange. They were varied within a physically meaningful range (~ 0.5 - 0.9) based upon previously reported values [7]. The heat transfer model affected the entire pressure trace and was tuned mainly by adjusting the average wall temperature. Again, a physically reasonable value (400 K) was chosen for this tuning knob.

The Wiebe function was tuned in order to match the combustion pressures. As with the previous two tuning knobs, physically reasonable values were chosen for the start of combustion (1.25° before TDC) and the burn duration (56°), and the a (5) and m (1.81) coefficients are similar to previously published data [7] [16].

In order to fully define the thermodynamic state of an ideal gas mixture, the composition of the gas mixture must be known along with two independent thermodynamic properties [24]. Since at any given crank angle the cylinder volume can be easily calculated from the engine's geometry, if the pressure is known then the thermodynamic state of the cylinder gases can be fully defined once the mass of the gas mixture and the mole fractions of the constituent species are known. Although the experimental setup used for this work did not permit the direct measurement of these two items, they could, using the methods described in the previous section, be calculated with reasonable accuracy. Therefore, since the simulated and experimental pressure curves are nearly overlapping, this suggests that the average thermodynamic properties of the cylinder gases are being faithfully modeled in the simulation.

However, since large temperature gradients can exist in the cylinder, and since the formation of NO is so heavily influenced by temperature, a mere knowledge of the average

thermodynamic properties will not suffice for predicting the exhaust concentration of nitric oxides. In order to better account for this spatial variation of temperature in the engine, a three-zone model was used for the combustion process when NO is formed.

Figure 12 shows how each zone varies in temperature throughout the combustion process. It is apparent that there can be prodigious disparities in the temperatures of the various zones. This emphasizes the need for a multi-zone model. If the one-zone average temperature were used, there would be a dramatic under-prediction of NO formed. Also, as will be illustrated more forcefully later on, even relatively modest temperature differences such as that existing between the adiabatic core and the burned zone can yield significantly different predictions for NO formation.

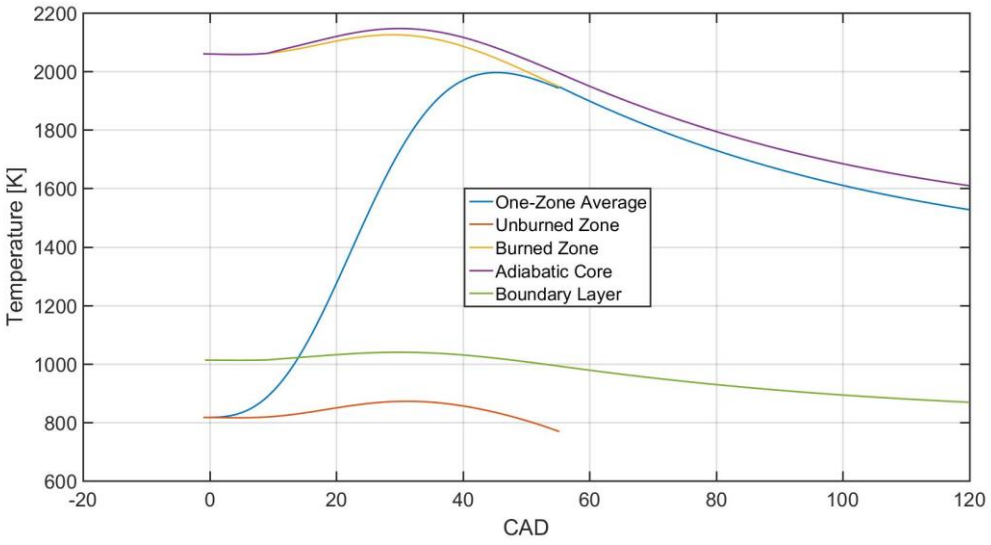

Figure 12: Temperatures of Different Zones During the Combustion and Expansion Processes

After combustion, when all the cylinder mass has moved to the burned zone, the three-zone model collapses to a two-zone model. The adiabatic core and boundary layer

temperatures are calculated throughout the expansion process in case temperatures are still hot enough for NO to be formed. For the current work, it was found that NO formation was negligible for most of the expansion process.

A comparison of Figure 12 with Figure 13 below shows that most of the NO is formed during the middle of combustion, where temperatures are highest. Near the end of combustion, the adiabatic core temperature has sufficiently dropped such that little NO is able to form, and even though the adiabatic core temperature is high enough near the beginning of combustion to produce NO, the mass of the adiabatic core at this time is so small that NO formation is minimal. There is an initial, non-zero NO concentration due to the fact that residual burned gases from the previous cycle are present at the start of combustion.

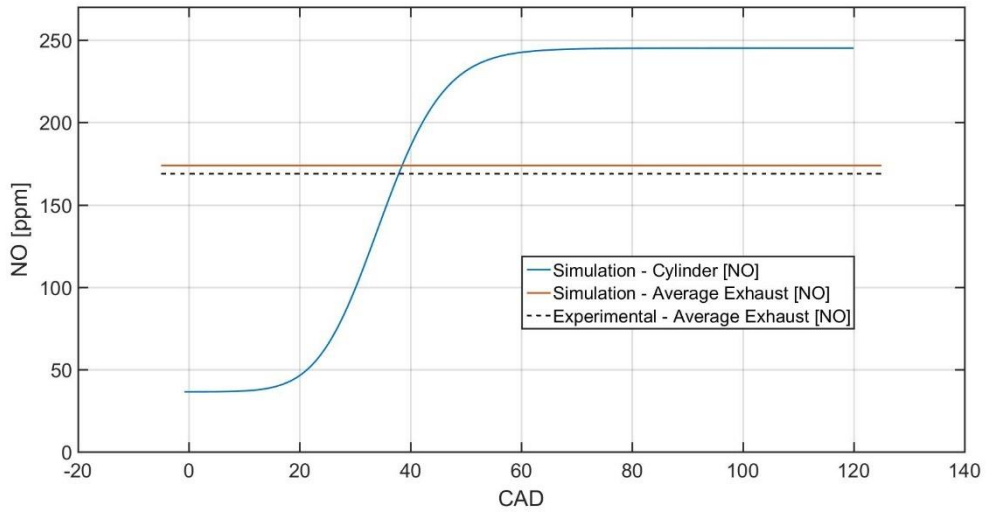

Figure 13: Concentration of NO during the Combustion and Expansion Processes, along with the Simulated and Measured Steady-State Average Exhaust Concentrations

The two horizontal lines in Figure 13 illustrate an additional challenge in calculating nitric oxide emissions from two-stroke engines. The NO concentration in the

cylinder at the end of the expansion process, just before the exhaust valve opens, will not be the concentration measured by an emissions analyzer. This is due to the fact that in two-stroke engines, the intake and exhaust ports are open at the same time for a significant amount of the cycle. For the Ajax engine used in this work, gas exchange comprises exactly one third of the engine cycle, and the intake and exhaust ports are open simultaneously for 70% of the gas exchange process. For this reason, much of the intake air (37% in the current simulation) is short-circuited, thus diluting the burned gases in the exhaust. The simulation must account for this dilution of NO in order to compare the simulated results with experimental measurements. This underscores the importance of a good scavenging model in addition to the NO formation calculations.

The average simulated and experimental exhaust NO concentrations depicted in Figure 13 above are reproduced below in Figure 14. While Figure 13 highlights the formation of NO in the cylinder and its dilution by short-circuited air, Figure 14 focuses on the variability of the experimentally measured nitric oxide concentrations. In both plots, the solid red line and dashed black line mark the average simulated and experimental results, respectively. In Figure 14 the first standard deviation of the measurements is marked by the dotted black lines above and below the average. The blue line represents the raw experimental NO_x measurement, sampled every tenth of a second.

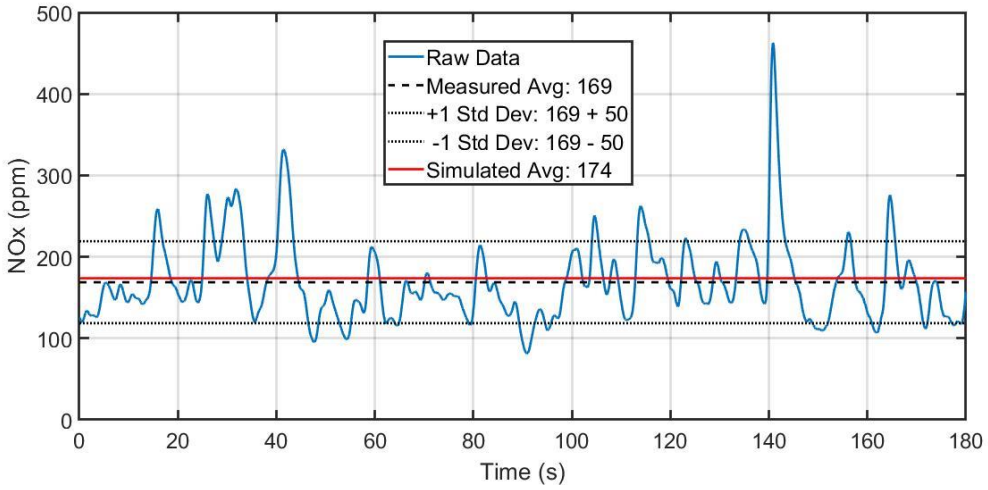

Figure 14: Simulated NO_x Prediction Compared to Experimental NO_x Measurements

Due to the inherent randomness of certain aspects of internal combustion engines, e.g. turbulent flow, there will always be some variation in engine behavior from cycle to cycle. The engine used for the current work is a particularly susceptible victim to cyclic variability because it is a lean burning, single cylinder engine. This variability will be addressed in more detail further on, but it can presently be noted that the average simulated nitric oxide concentration is quite close to the measured average value, and well within the first standard deviation.

This encouraging result indicates that the average exhaust NO concentration is being calculated about as accurately as could be expected from a zero-dimensional simulation. However, this degree of accuracy may be difficult to consistently obtain. Figure 15 and Figure 16 show the simulated vs. experimental values for CO_2 and O_2 exhaust concentrations, respectively, and the agreement is not as impressive. This could indicate that the degree of accuracy of the NO_x prediction is somewhat fortuitous in this

case. Furthermore, the following sections (4.2 and 4.3) show that the presence of significant cyclic variability makes it dubious that any single cycle simulation could give repeatably accurate emissions predictions.

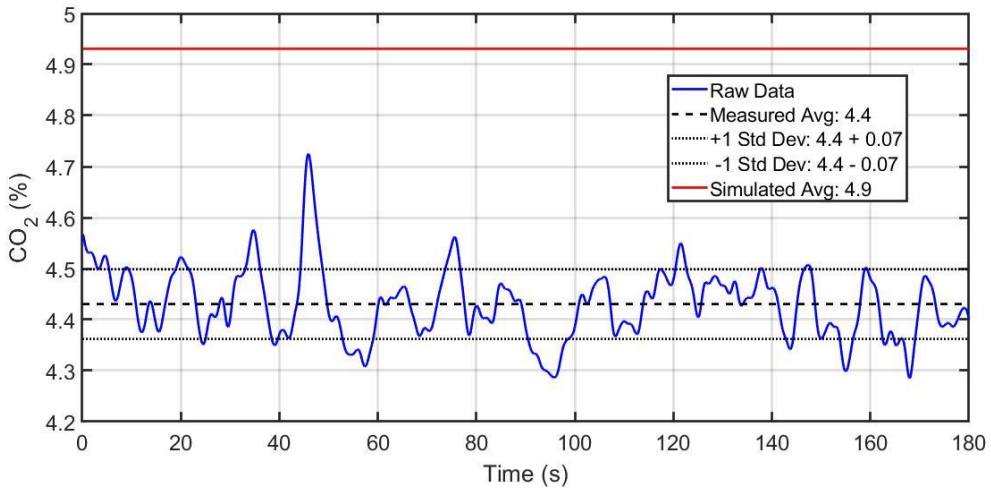

Figure 15: Simulated CO_2 Prediction Compared to Experimental CO_2 Measurements

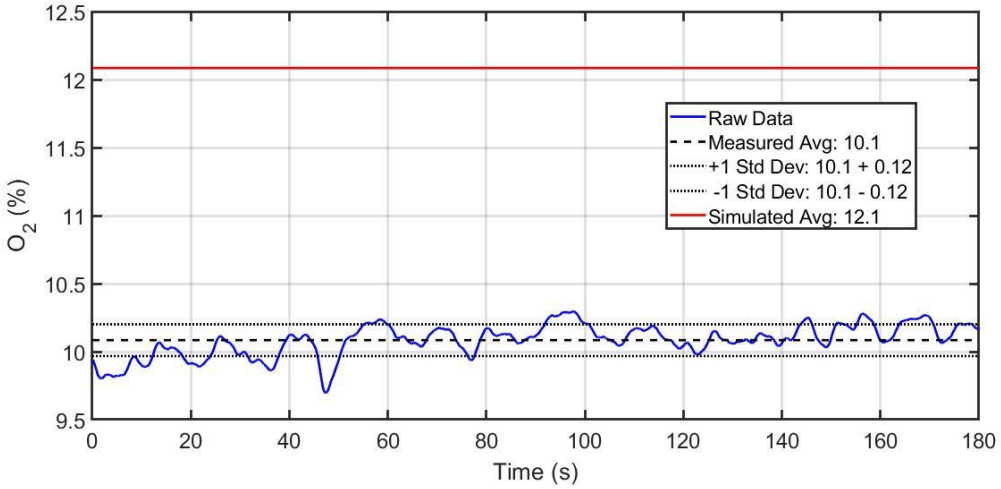

Figure 16: Simulated O_2 Prediction Compared to Experimental O_2 Measurements

4.2. Sensitivity Analysis

4.2.1. Varying TER

The first item examined in the sensitivity analysis was TER. Of all the items, the simulation was found to be most sensitive to TER. Figure 17 shows the exponential relationship between TER and predicted NO_x. The TER was varied ± 3%, 6%, and 9% from the base case value.

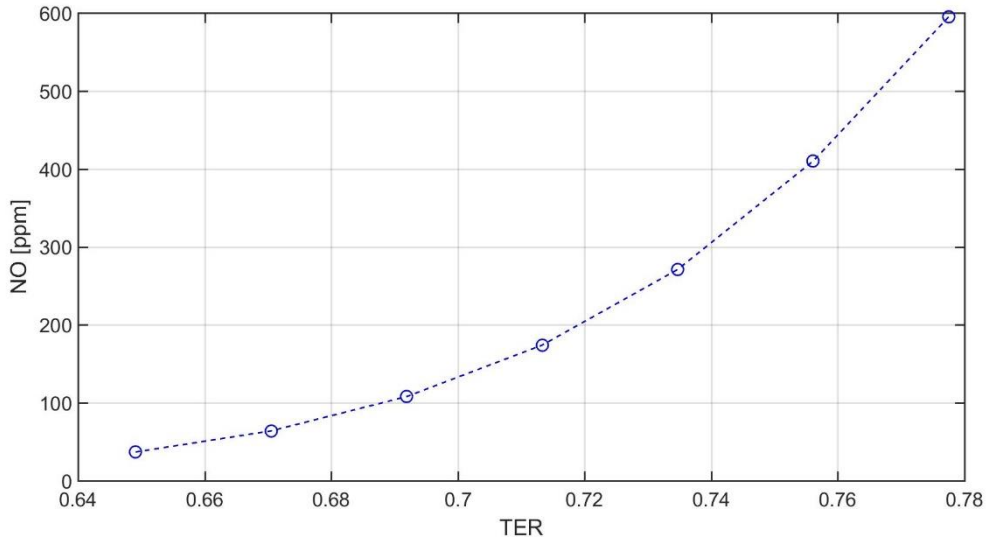

Figure 17: Exhaust NO_x Concentration as a Function of TER

The reason for this exponential trend is the change in adiabatic core temperature with changing TER, shown in Figure 18. As the equivalence ratio richens toward stoichiometric, there is less air acting as a diluent in the combustion reaction, and thus the flame temperature increases.

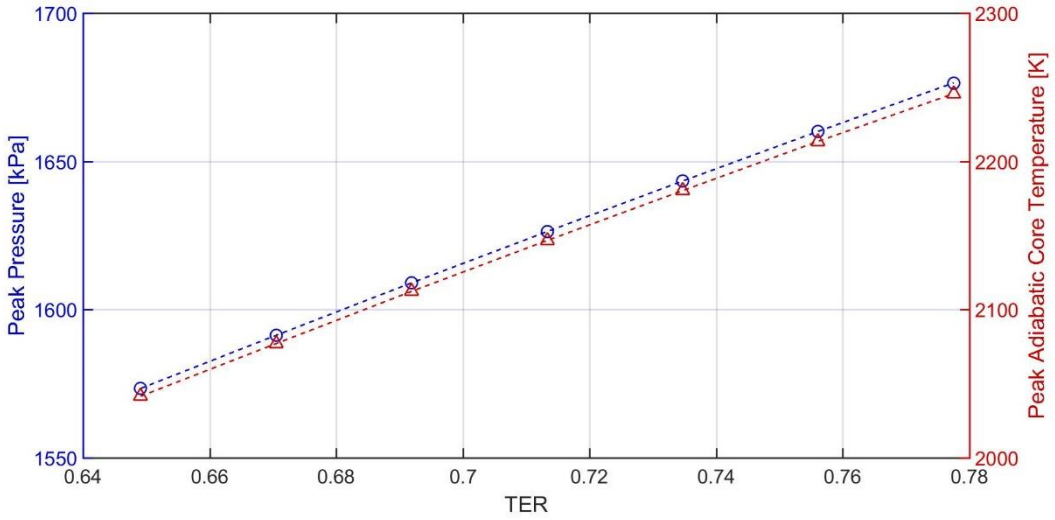

Figure 18: Peak Pressure and Peak Adiabatic Core Temperature as a Function of TER

The direct, linear relationship between adiabatic core temperature and TER applies throughout the combustion and expansion processes, and not merely at the location of peak temperature. Figure 19 shows that changing TER will basically effect a linear offset in the adiabatic core temperature throughout the combustion and expansion processes (i.e., the whole curve will be moved up or down).

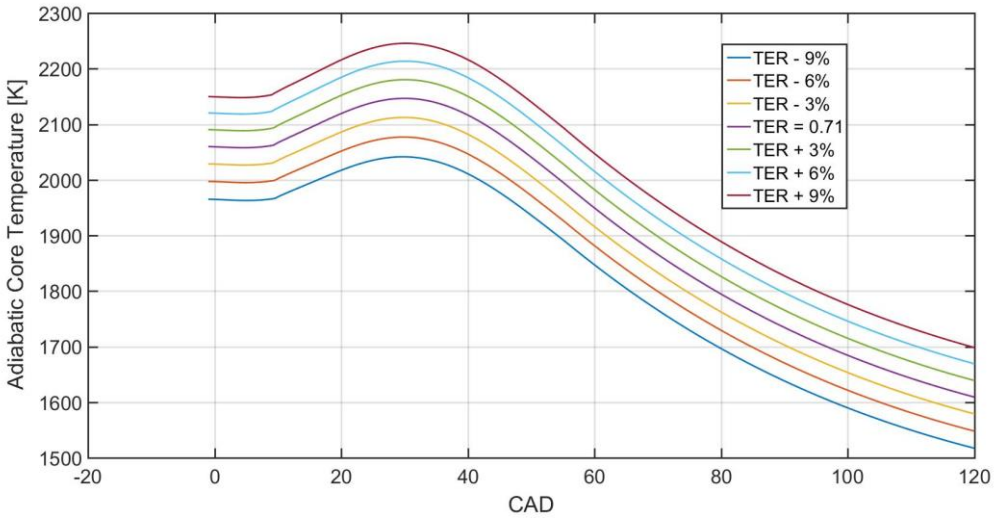

Figure 19: Adiabatic Core Temperature as a Function of Crank Angle for Varying TER

It is important to note that linear changes in the adiabatic core temperature result in exponential changes in the NO_x prediction. It is also noteworthy that peak pressure trends linearly with the adiabatic core temperature, which is an intuitive result given the direct relationship between pressure and temperature in the ideal gas law. Pressure is not directly an input in the simulation's NO formation sub-model, but its linear relationship with adiabatic core temperature, and thus its exponential relationship with NO formation, will be treated in the following chapter due to its implications concerning cyclic variability.

The important phenomenon of linear changes in adiabatic core temperature effecting exponential changes in NO formation is due to the exponential terms in the chemical kinetics equations governing the Zeldovich mechanism. The current work found the first reaction to be particularly important for the conditions studied.

The third reaction in the Zeldovich mechanism was found to be negligible for the conditions studied in this work. The second reaction was found to be significant for the current work, but the simulation was not sensitive to changes in the rate constants of the second reaction. For instance, a 500% increase in k_{2f} resulted in merely a 1% increase in the predicted exhaust NO_x concentration. On the other hand, any percentage change in k_{1f} led to roughly an equal percentage change in the predicted NO_x, as Figure 20 illustrates. This coincides with other work stating the first reaction to be the rate limiting reaction [10] [16].

For the temperature regions studied in the current work, k_{2f} was also found to be less sensitive to temperature change than k_{1f}. For instance, in the range of peak adiabatic core temperatures displayed in Figure 18, k_{1f} increased by 460% while k_{2f} increased by only 30%. At lower temperatures, k_{2f} is even less sensitive to temperature changes. It is important to emphasize, however, that the second reaction was still important and should not be neglected, even though it was not sensitive to changing temperatures. If the second reaction was neglected entirely, it resulted in a 60% reduction in the simulated exhaust NO_x concentration.

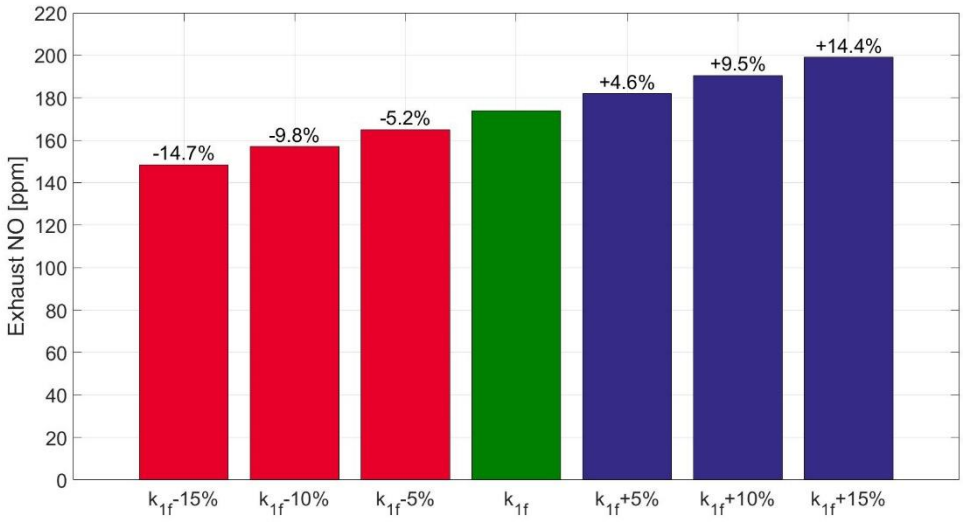

Figure 20: Bar Graph Showing the Change in NO_x Concentration for Changing k_{1f}

Figure 20 shows the exhaust NO_x concentration that would be calculated by the cycle simulation if the forward rate constant of the first reaction had been altered by a certain percentage. The values on the x-axis list the percentage that k_{1f} was altered, and the values above the bars indicate the percentage that the predicted NO_x changed from the base case (green bar). For instance, a 10% increase in k_{1f} resulted in a 9.5% increase in the simulated exhaust NO_x concentration.

Figure 21 shows k_{1f} as a function of the peak adiabatic core temperatures used in Figure 18. This figure, taken together with Figure 18 and Figure 20, demonstrates the reason why NO_x is so sensitive to TER at this operating condition. Figure 18 shows that higher TER leads to higher adiabatic core temperatures. Figure 21 shows that higher adiabatic core temperatures lead to exponentially higher values of the forward rate constant for the first reaction in the Zeldovich mechanism. Finally, Figure 20 indicates that since any percentage change in this rate constant leads to roughly the same percentage

change in overall NO production, exponential changes in the rate constant will lead to exponential changes in NO production.

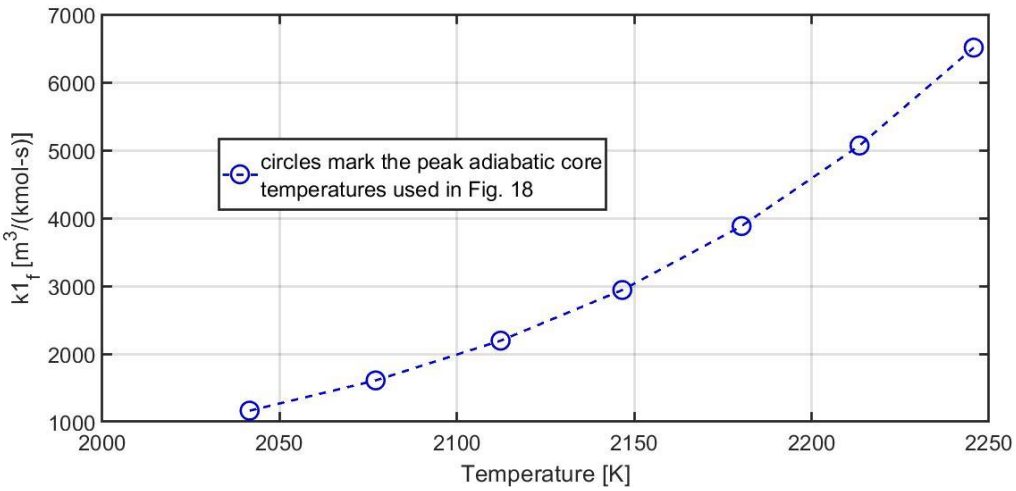

Figure 21: k_{1f} as a Function of Temperature

The link between TER and NO_x, described in the above paragraph, is illustrated simply in Figure 22 below.

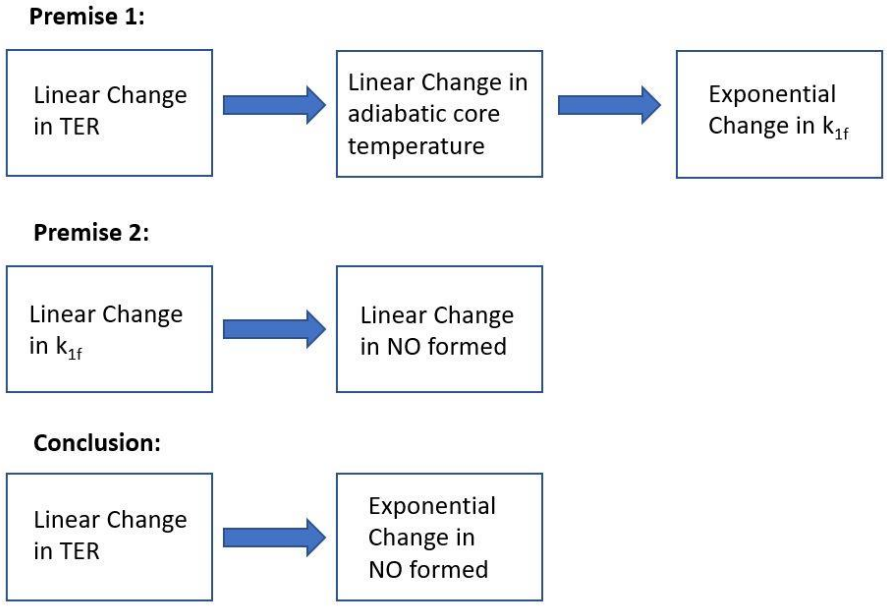

Figure 22: Flow Chart of Linear Changes in TER Leading to Exponential Changes in NO_x

The sensitive exponential relationship between TER and NO_x presents a difficult challenge for zero-dimensional modeling because the trapped gas mixture is assumed to be homogeneous and thus have the same equivalence ratio everywhere, but this idealization will be of varying validity for different engines. This assumption is of yet on questionable ground for the Ajax engine used in the current work. Without more detailed fluid mechanics calculations, it is difficult to judge the degree to which the trapped mass is homogeneous at the time of spark, but Figure 17 shows that any stratification could have non-trivial consequences for NO_x predictions.

4.2.2. Varying x_b

The second item examined in the sensitivity analysis was x_b. Figure 23 shows the effect of varying xb on the NO_x prediction. Similar to TER, x_b was varied ± 3%, 6%, and 9% from the base case value. The simulation was not quite as sensitive to changes in x_b as it was to TER, and in this case there was an inverse relationship between the two.

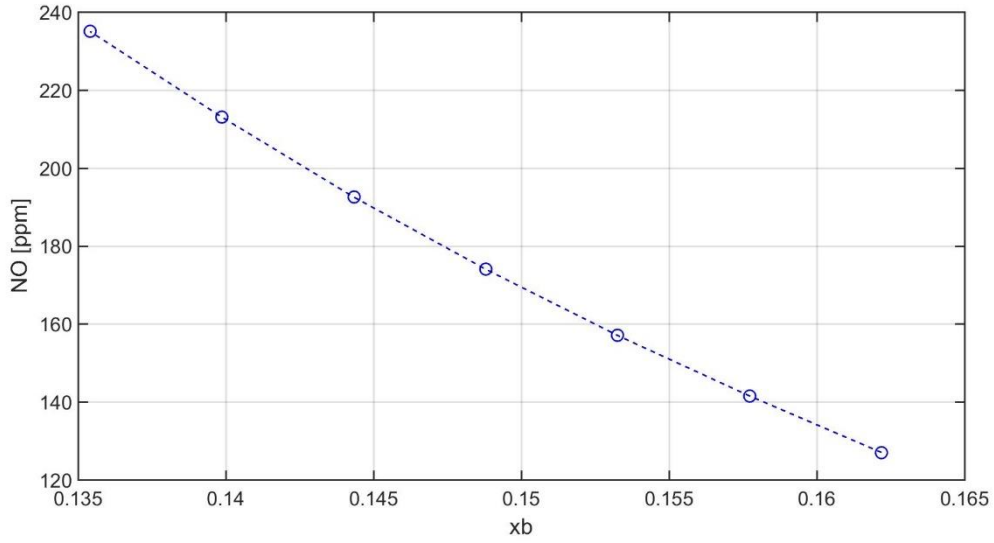

Figure 23: Exhaust Concentration of NO_x as a Function of x_b

The relationship between NO_x and x_b appears to be nearly linear, but this is just a small section of an exponential relationship. This is because the reason why NO_x changes with x_b is again because temperatures change with x_b, shown in Figure 24. As the fraction of residual gases in the cylinder is increased, the trapped charged becomes more diluted, so flame temperatures drop. Conversely, when x_b decreases, there is less diluent to suppress the flame temperature.

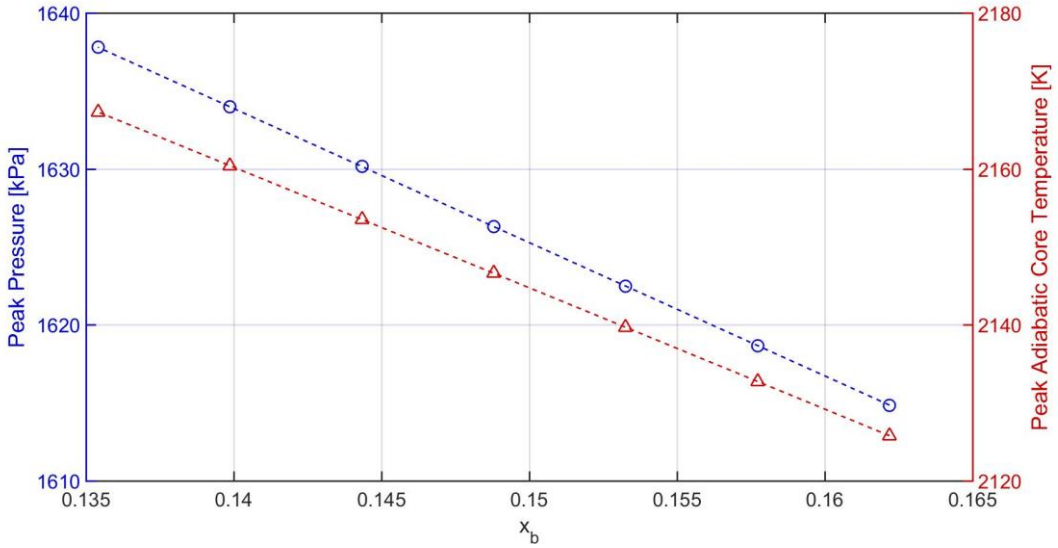

Figure 24: Peak Pressure and Peak Adiabatic Core Temperature as a Function of x_b

Again, the peak pressure trends nearly linearly with adiabatic core temperature, and this will be important in the following chapter on cyclic variability. Also, similar to TER, this linear relationship between adiabatic core temperature and x_b exists throughout the combustion and expansion processes. A change in x_b effects a linear offset in combustion temperatures, as Figure 25 shows.

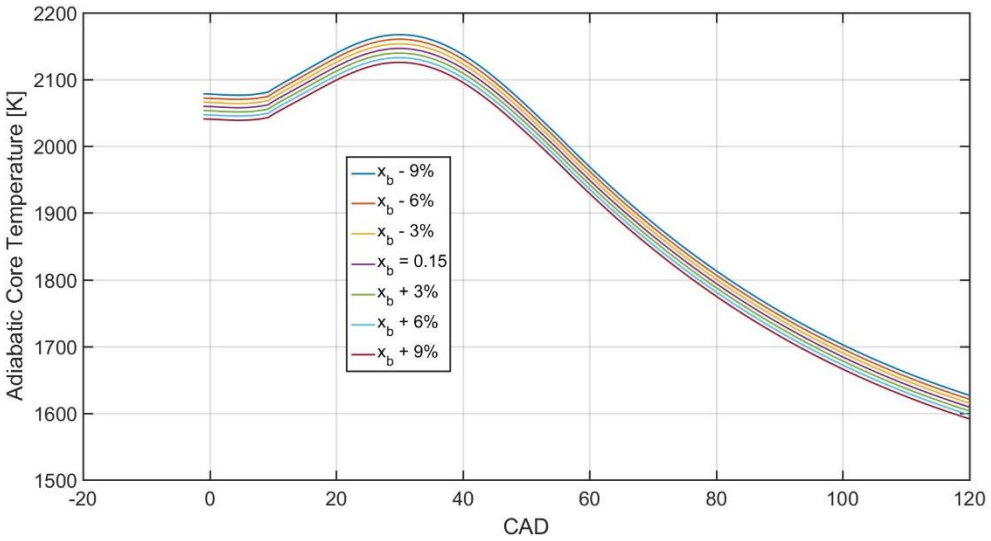

Figure 25: Adiabatic Core Temperature as a Function of Crank Angle for Varying x_b

A comparison of Figure 24 and Figure 25 with their TER counterparts (Figure 18 and Figure 19) shows that the change in temperature is more pronounced for changing TER than for changing x_b. This explains why the simulation is more sensitive to TER than to x_b. Linear changes in either TER or x_b will result in linear changes in adiabatic core temperatures, which result in exponential changes in k_{1f}, which then result in exponential changes in NO formed during the cycle. However, linear changes in TER produce steeper linear changes in adiabatic core temperatures than does x_b. Linear curve fits to Figure 18 and Figure 24 show that the peak adiabatic core temperature changes by 11.4 K for each percentage change in TER, but it only changes by 2.3 K for each percentage change in x_b. This is illustrated more clearly in Figure 26 below.

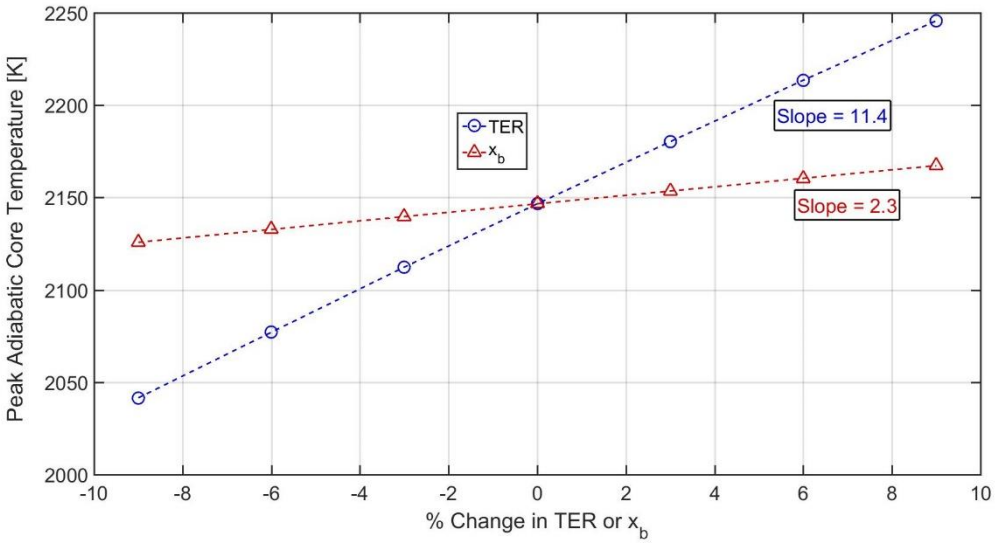

Figure 26: Sensitivity of the Peak Adiabatic Core Temperature to Percentage Changes in TER and x_b

The sensitivity analysis for x_b shows that, although not as important as TER, the value of x_b does have a significant impact on the predicted NO_x concentration. The main factor that affects the simulated x_b is the scavenging model, and zero-dimensional modeling of scavenging is notoriously difficult. However, the relatively mild relationship between x_b and NO_x suggests that the perfect mixing model may be sufficient for various applications where a ballpark estimate of NO_x is needed.

4.2.3. Varying SBT

The final item examined in the sensitivity analysis was the SBT. Similar to TER and x_b, the SBT affects the NO_x prediction through its effect on combustion temperatures. In contrast to TER and x_b, however, the SBT seems to affect combustion temperatures in more than one manner. The following sensitivity analysis will attempt to identify the various ways SBT affects NO formation and quantify the contribution from each.

To begin, Figure 27 shows the relationship between the predicted exhaust NO_x concentration and SBT. The SBT was varied ± 5, 10, and 15 K from the base case value of 314.5 K, and the resulting trend is clearly exponential in this range.

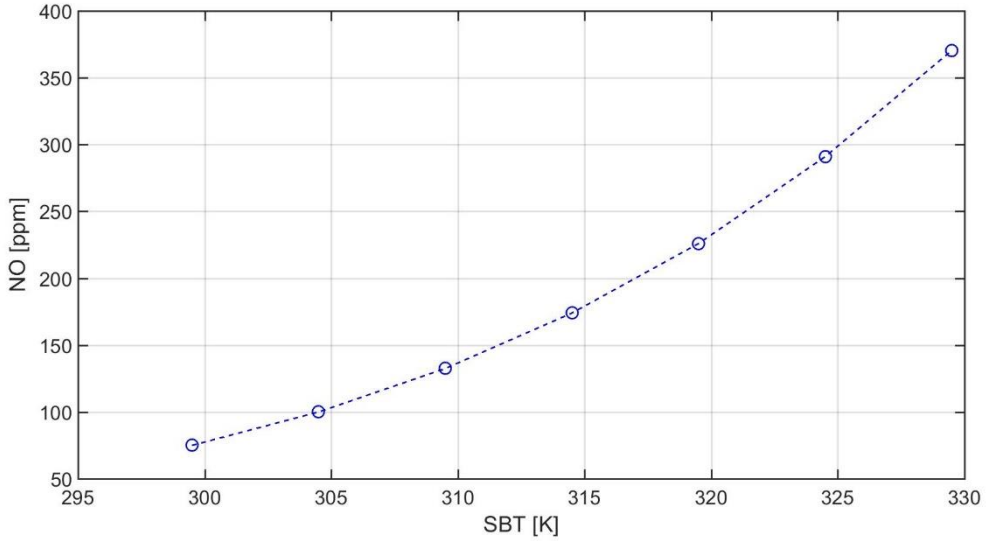

Figure 27: Exhaust Concentration of NO_x as a Function of SBT

Before attempting to enumerate the factors behind this exponential relationship, it is emphasized once again that changes in the NO_x prediction are due to changes in the adiabatic core temperature. Figure 28 shows the direct relationship between SBT and the adiabatic core temperature. The following plot, Figure 29, shows that as with TER and x_b, this linear relationship persists throughout combustion and expansion.

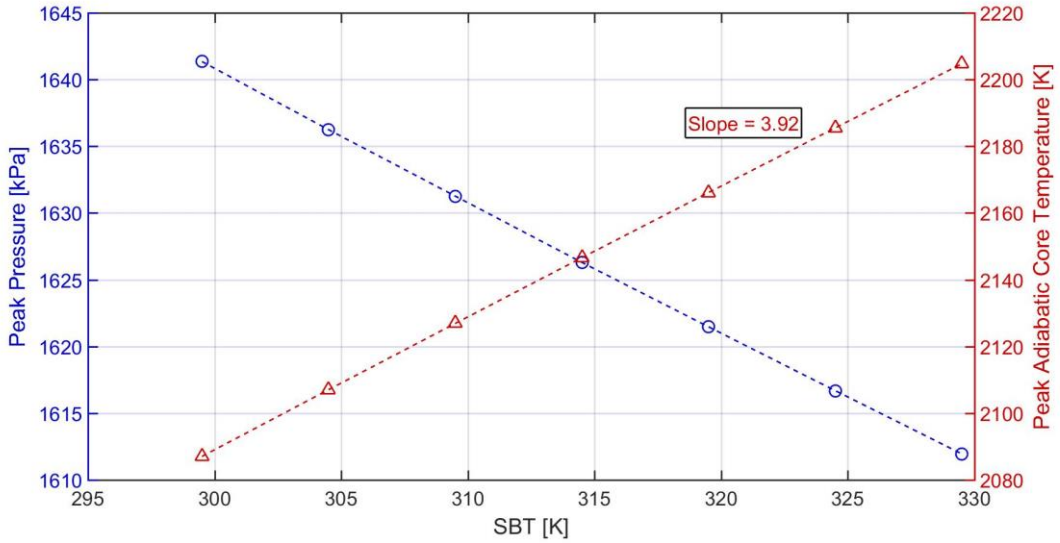

Figure 28: Peak Pressure and Peak Adiabatic Core Temperature as a Function of SBT

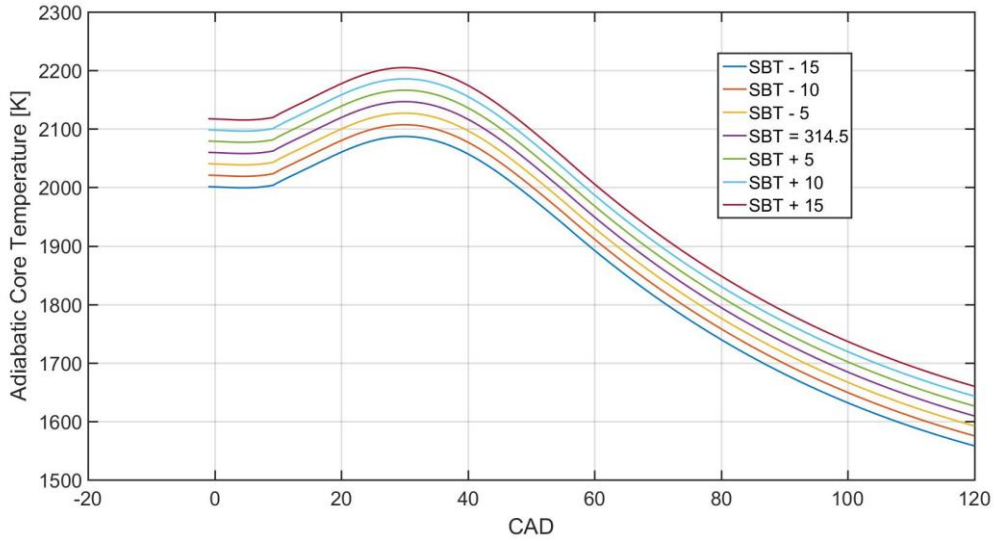

Figure 29: Adiabatic Core Temperature as a Function of Crank Angle for Varying SBT

A striking result appears concerning peak pressure in Figure 28. Whereas for TER and x_b, the pressure was directly, linearly related to combustion temperatures, now pressure is inversely, linearly related to combustion temperatures. This initially counter-

intuitive result can be understood since although pressure is directly related to temperature in the ideal gas law, it is also directly related to the trapped mass in the cylinder. For higher SBT, the fresh mass delivered each cycle is less, and the resulting reduction in trapped mass has a more powerful effect on cylinder pressures than do the elevated temperatures. Figure 30 shows how the trapped mass trends with SBT. This result will be of interest in the next chapter concerning cyclic variability.

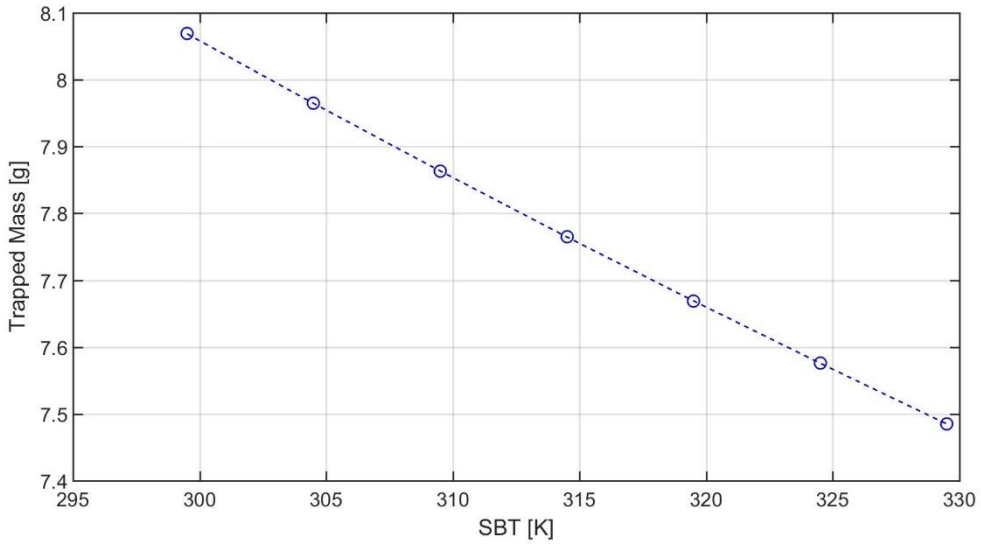

Figure 30: Trapped Mass as a Function of SBT

The linear increase in adiabatic core temperatures with SBT shown above seems to be driven by the following three factors:

1. Higher SBT leads to higher temperatures at EPC and just before combustion. This in turn, leads to elevated combustion temperature, because of the elevated reactant temperature. The converse is true for lower SBT.
2. Higher SBT goes together with lower density of intake air. If the intake air is less dense, there will not be as much fresh air delivered to the cylinder each cycle,

which will effectively richen the trapped charge. This increase in TER will increase combustion temperatures, as argued earlier. Conversely, lower SBT leads to lower TER.

3. There is a slight inverse trend between x_b and SBT, indicating an improvement in scavenging at higher intake temperatures. This seems to be due to the fact that the exhaust mass flow rate for much of the exhaust blow down period is limited because the flow is choked. The mass flow rates for exhaust blowdown do not vary significantly as SBT is changed. This fact, in conjunction with the inverse relationship between trapped mass and SBT shown in Figure 30, means that as SBT increases, a higher fraction of trapped mass is exhausted during exhaust blowdown.

Evidence for the three factors listed above will now be provided, as well as an attempt to roughly quantify the relative contribution of each factor to adiabatic core temperature.

Beginning with evidence for the first factor in the list, Figure 31 shows how the temperatures at EPC and the start of combustion (SOC) both increase linearly with SBT. This is a very predictable result. For every 1 K increase in SBT, the temperatures at EPC (T_{EPC}) and SOC (T_{SOC}) increase by 1.1 K and 1.5 K, respectively.

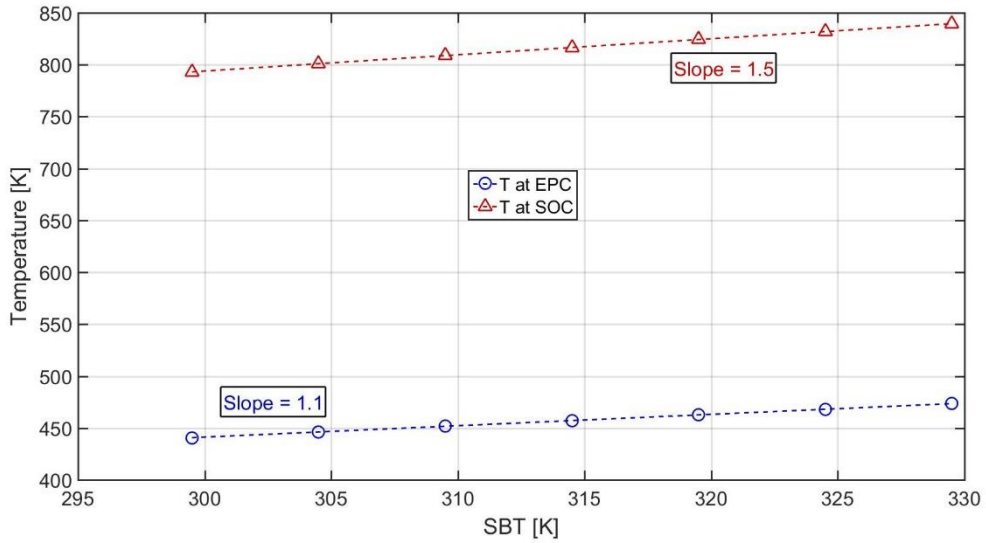

Figure 31: T_{EPC} and T_{SOC} as a Function of SBT

Figure 32 presents evidence for the second and third factors in the list. For every 1 K increase in SBT, TER increases by 0.23% and x_b decreases by 0.17%. As seen earlier, both of these trends will lead to a direct relationship between SBT and adiabatic core temperature.

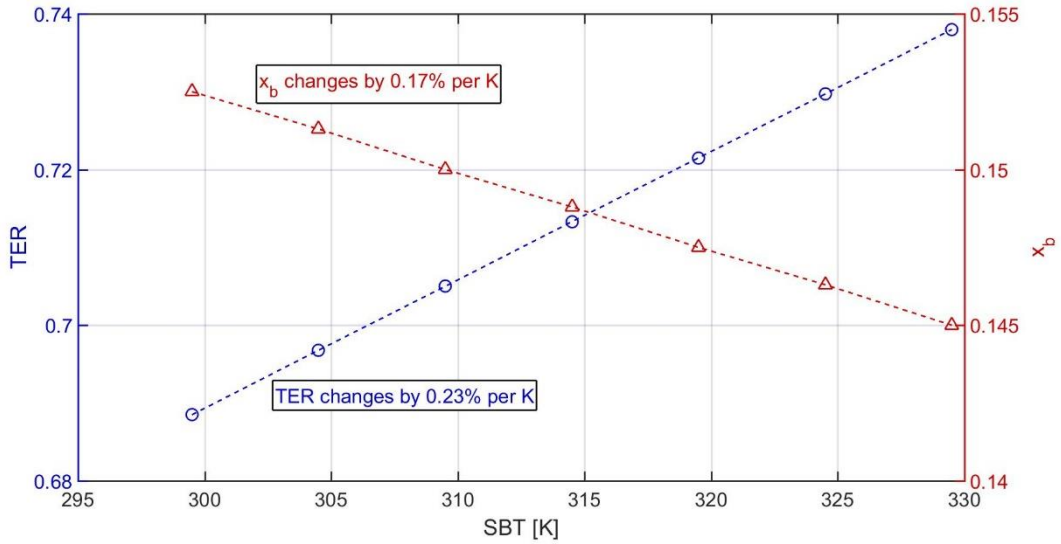

Figure 32: Sensitivity of TER and x_b to Changes in SBT

It has now been shown that changes in SBT cause linear changes in T_{SOC}, TER, and x_b. It has also been shown that for every 1 K increase in SBT, T_{SOC} increases by 1.5 K, TER increases by 0.23%, and x_b decreases by 0.17%. These factors together, as shown in Figure 28, led to a 3.92 K increase in peak adiabatic core temperature for every 1 K increase in SBT.

Having identified these three factors, and the fact that their cumulative effect is a 3.92 K increase in adiabatic core temperature per 1 K increase in SBT, the relative impact of each factor remains to be seen. In order to isolate the effect of each factor, the adiabatic flame temperature (T_{AF}) was successively calculated as a function of T_{SOC}, TER, and x_b. When T_{AF} was calculated as a function of one factor, the other two factors were held constant at the base case values. For instance, when T_{SOC} was varied, TER and x_b were held constant. In this way the effect of each factor could be isolated.

In this analysis, T_{AF} is being used as a proxy for the adiabatic core temperature throughout combustion and expansion. In other words, it is assumed that whatever increase or decrease occurs in T_{AF}, the same increase or decrease will occur for the adiabatic core temperature at every crank angle degree. This rationale is supported by the fact that Figure 19, Figure 25, and Figure 29 all show that changes in TER, x_b, and SBT lead to a linear offset in the adiabatic core temperatures throughout the combustion and expansion processes. This offset is nearly the same at the beginning of combustion as it is everywhere else in combustion, and in this simulation, the adiabatic core temperature is initialized by the adiabatic flame temperature. Thus, it seems reasonable to use T_{AF} as a proxy for the adiabatic core temperatures, in order to identify the relative effects of

changing T_{SOC}, TER, and x_b. This is further reinforced by Figure 33, which shows that any change in the adiabatic flame temperature leads to nearly exactly the same change in peak adiabatic core temperature.

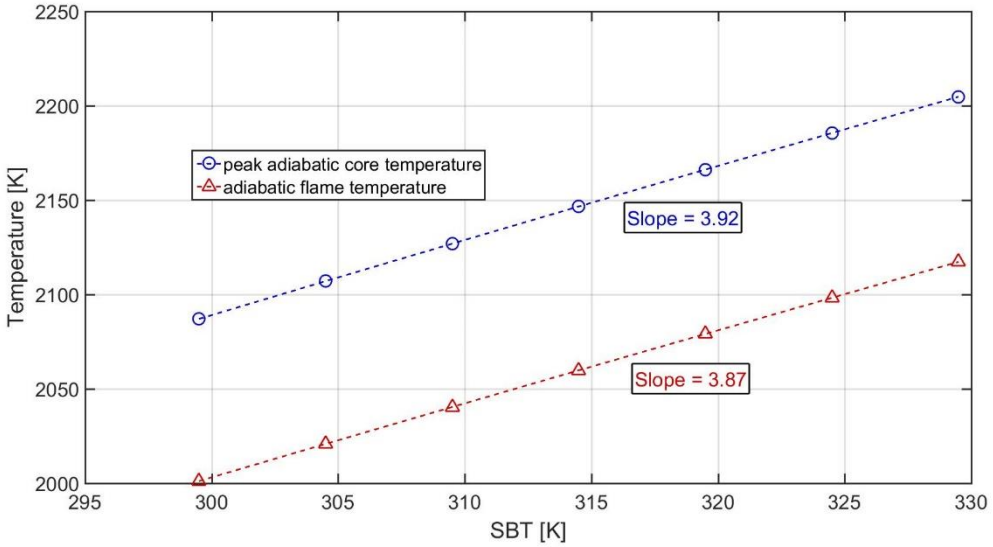

Figure 33: Adiabatic Flame and Peak Adiabatic Core Temperatures as a Function of SBT

Figure 34 and Figure 35 below show the results of this analysis: for every 1 K increase in T_{SOC} there was a 0.82 K increase in T_{AF}; for every 1% increase in TER there was a 9.83 K increase in T_{AF}; and for every 1% increase in x_b there was a 1.98 K decrease in T_{AF}. The values used for T_{SOC}, TER, and x_b in this analysis were chosen to roughly correspond to those that occur as SBT is varied ± 5, 10, and 15 K from the base case value.

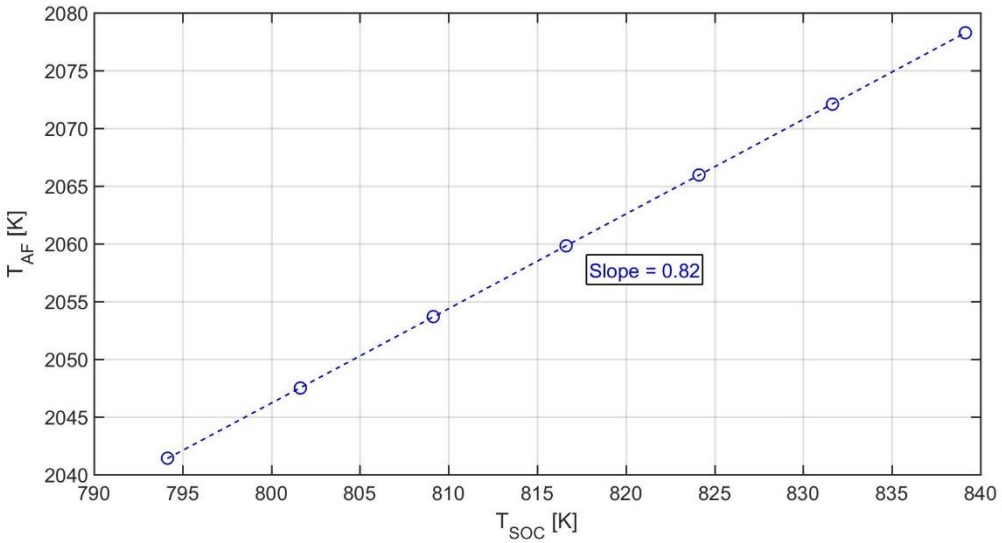

Figure 34: T_{AF} as a Function of T_{SOC}

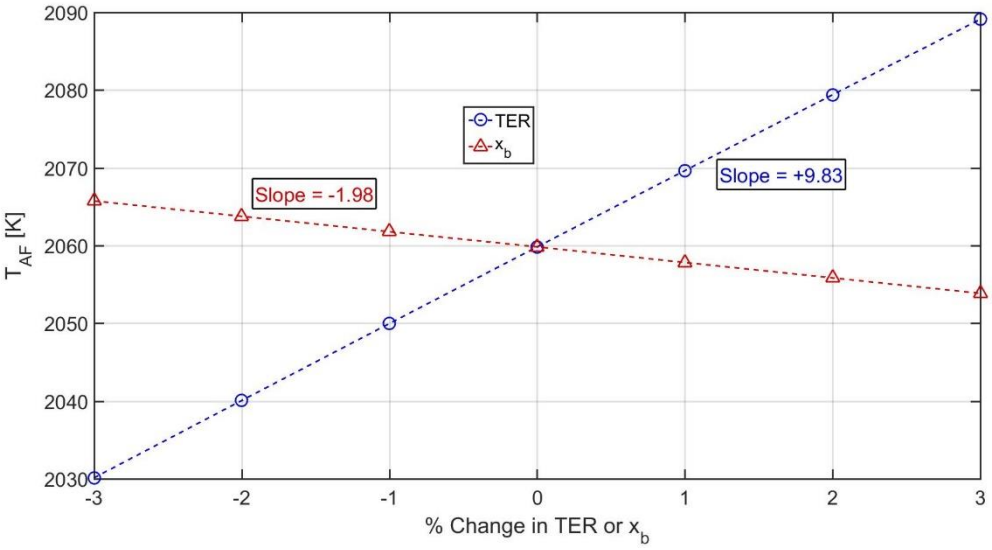

Figure 35: Sensitivity of T_{AF} to Percentage Changes in TER and x_b

Having isolated the effects of T_{SOC}, TER, and x_b, the relative contribution of each to the relationship between adiabatic core temperature and SBT can now be computed. Figure 33 shows that for every 1 K increase in SBT, T_{AF} increases by 3.87 K. The

following identifies what portion of that 3.87 K increase is due to each of the three factors, i.e., T_{SOC}, TER, and x_b.

Concerning the first factor, since T_{SOC} increases by 1.5 K for every 1 K increase in SBT, and T_{AF} increases by 0.82 K for every 1 K increase in T_{SOC}, it follows that rising T_{SOC} will cause T_{AF} to increase by 1.23 K for every 1 K increase in SBT. This is shown in equation (69) below.

$$\frac{\Delta 1.5\ K\ [T_{SOC}]}{\Delta 1\ K\ [SBT]} * \frac{\Delta 0.82\ K\ [T_{AF}]}{\Delta 1\ K\ [T_{SOC}]} = \frac{\Delta 1.23\ K\ [T_{AF}]}{\Delta 1\ K\ [SBT]} \tag{69}$$

Changes in T_{SOC} thus account for $\frac{1.23}{3.87}$ (or 32%) of the direct relationship between T_{AF} and SBT.

Concerning the second factor, since TER increases by 0.23% for every 1 K increase in SBT, and T_{AF} increases by 9.83 K for every 1% increase in TER, it follows that rising TER will cause T_{AF} to increase by 2.26 K for every 1 K increase in SBT. This is shown in equation (70) below.

$$\frac{\Delta 0.23\%\ [TER]}{\Delta 1\ K\ [SBT]} * \frac{\Delta 9.83\ K\ [T_{AF}]}{\Delta 1\%\ [TER]} = \frac{\Delta 2.26\ K\ [T_{AF}]}{\Delta 1\ K\ [SBT]} \tag{70}$$

Changes in TER thus account for $\frac{2.26}{3.87}$ (or 58%) of the direct relationship between T_{AF} and SBT.

Finally, concerning the third factor, since x_b decreases by 0.17% for every 1 K increase in SBT, and T_{AF} increases by 1.98 K for every 1% decrease in x_b, it follows that decreasing x_b will cause T_{AF} to increase by 0.34 K for every 1 K increase in SBT. This is shown in equation (71) below.

$$\frac{\Delta 0.17\%\ [x_b]}{\Delta 1\ K\ [SBT]} * \frac{\Delta 1.98\ K\ [T_{AF}]}{\Delta 1\%\ [x_b]} = \frac{\Delta 0.34\ K\ [T_{AF}]}{\Delta 1\ K\ [SBT]} \tag{71}$$

Changes in x_b thus account for $\frac{0.34}{3.87}$ (or 9%) of the direct relationship between T_{AF} and SBT.

The conclusions of the last several paragraphs are illustrated by Figure 36.

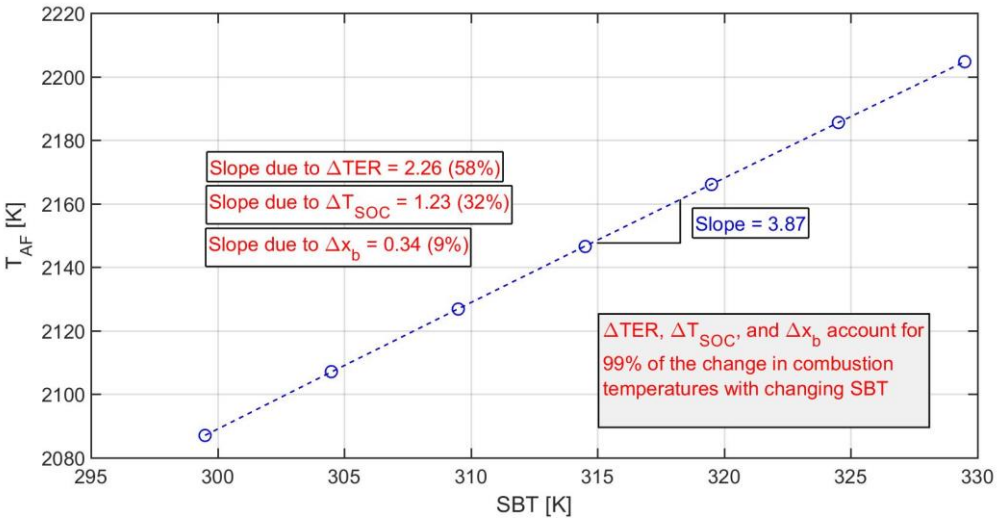

Figure 36: Contributions of TER, T_{SOC}, and x_b to the relationship between T_{AF} and SBT

It has been shown that there is a direct, linear relationship between SBT and adiabatic core temperatures, and that this drives a direct, exponential relationship between SBT and NO_x. The preceding analysis argues that roughly 99% of the increase in adiabatic core temperatures with SBT can be accounted for by changes in T_{SOC}, TER, and x_b. Furthermore, since the adiabatic core temperatures are what drive NO formation, this analysis also suggests that changes in T_{SOC}, TER, and x_b account for roughly all of the change in NO_x with SBT.

Not only does this demonstrate that nearly all the increase in NO_x is attributable to three known factors, it also shows the relative importance of each factor. This knowledge could be very useful for future designs of similar engines. For instance, if fuel-intake was controlled so that TER could be held constant as the SBT was increased 5 K from the base case, this would result in reducing NO_x by nearly 80% compared to letting to TER increase!

4.3. Relationship of Cyclic Variability to the NO_x Prediction

In the previous two chapters, the simulation was described to be validated by matching an average of 1,460 cycles. In this way, the simulation describes the behavior of an "average" cycle, but the notion of "average" is not as concrete as it may initially seem. Thus far, since in-cylinder pressure is seen as the most important experimental measurement available, an "average cycle" has been used to mean the cycle that has the average pressure curve; this is computed, for any given crank angle, as the average of all the pressure curves at that crank angle.

One problem with this method, however, is that the average cycle, calculated in this way, is a fictitious cycle, and there may be no real cycle that demonstrated "average" behavior. Another and more significant problem with this method for predicting NO_x, is that the average cycle in terms of pressure may not be the average cycle in terms of other engine parameters. For the purposes of this work, the average cycle in terms of pressure behavior may not be very similar to an average cycle in terms of NO_x production.

Indeed, evidence has been shown for this already in the previous chapter. Figure 18, Figure 24, and Figure 28 showed that peak pressure trended linearly with adiabatic

core temperature, which increased exponentially with NO_x. This would suggest that NO_x is non-linearly related to pressure, just as it is to temperature. These plots also showed, however, that there can be either direct or inverse relationships between pressure and temperature, depending on what type of cyclic variability is occurring.

Pressure changes were attributable to changes in either the amount or composition of trapped mass. If mass stayed nearly the same, but the composition varied, then pressure was directly related to temperature, as Figure 18 and Figure 24 showed. On the other hand, Figure 28 showed that changes in the amount of trapped mass could overcome the effects of varying mixture composition, and drive an inverse relationship between pressure and temperature. Thus, it is not immediately obvious whether a simulation, validated by matching an average pressure curve, would over- or under-predict the exhaust NO_x concentration.

There is evidence from the experimental data as well that an average cycle in terms of NO_x production may be difficult to obtain. Figure 14 showed that over the course of a three-minute sampling period, there was considerable variation in the measured exhaust NO_x concentration. The experimental pressure measurements also reveal large variations in the cylinder pressure from cycle to cycle. As reported in Table 2, the COV of IMEP for the 1,460 cycles measured was about 9%. Figure 37 illustrates this variability in the first 40 consecutive individual cycles of the 1,460 cycles measured.

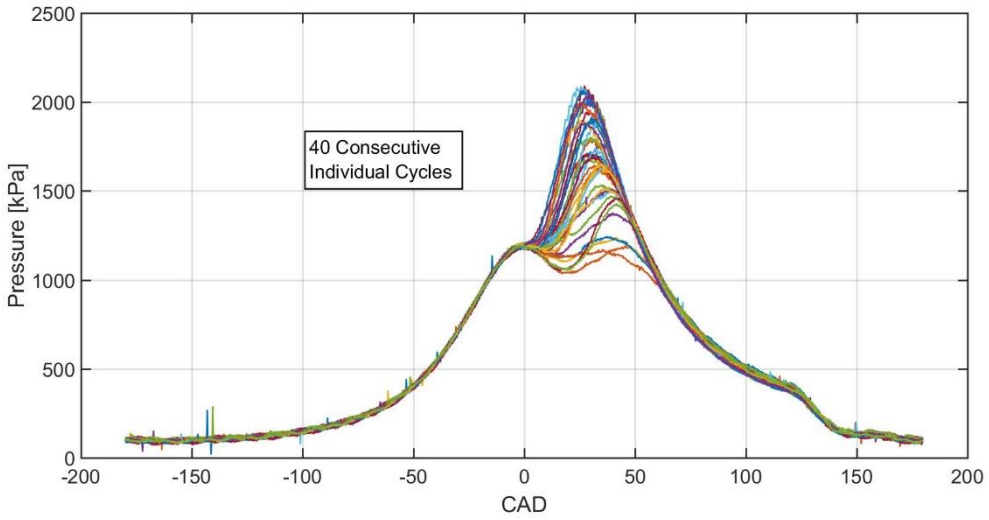

Figure 37: Cyclic Variability of Cylinder Pressures

The difficulties in dealing with cycling variability will be managed differently depending on the level of accuracy desired in the simulation, as well as the extent of variability present in a particular engine. However, since cyclic variability is a statistical phenomenon, caused by random fluctuations, it cannot be accounted for simply by increasing the resolution of the simulation for one cycle. The results presented in the current work indicate that three-dimensional simulations would be susceptible to the same issues as their zero-dimensional counterparts. Even the most perfect direct numerical simulation (DNS), considering all the chemical reactions in the GRI-mechanism, would be susceptible to producing erroneous results if it was validated by matching a misleading "average" cycle.

For this reason, a statistical model, coupled with zero-dimensional simulations, could be more useful. For instance, several zero-dimensional models could be validated by matching the pressure curves of different individual cycles. These pressure curves

would be real, not fictitious averages. Then, the NO_x prediction from each individual cycle could be averaged to estimate the average exhaust NO_x concentration. In this way, the problems that arise from the non-linear relationship between pressure and NO_x would be side-stepped. The computational cost of this method would be prohibitive for a high-resolution simulation like CFD, but it would be feasible with zero-dimensional simulations. In this manner, for the same computational cost, multiple lower resolution simulations might be able to achieve better results than a single higher resolution simulation.

5. CONCLUSIONS

A zero-dimensional thermodynamic cycle simulation was developed to model the behavior of an Ajax E-565, an IC engine of similar design to integral compressor engines. Experimental data were collected for the Ajax E-565 in order to tune and validate the simulation. The simulation was tuned to very closely model the average experimentally obtained in-cylinder pressure trace. Once the simulation was validated in this respect, a NO_x prediction sub-model using the extended Zeldovich mechanism was added in order to predict the concentration of NO_x in the exhaust gases, based upon the combustion temperatures calculated by the simulation. Excellent agreement was obtained between the simulated and measured exhaust NO_x concentrations.

A parametric sensitivity analysis was conducted to examine how the NO_x prediction would change in the presence of changing TER, x_b, and SBT. It was found that as TER was increased toward the stoichiometric value, a higher percentage of the trapped charge reacted, causing combustion temperatures to increase linearly. These linear increases in temperature caused exponential increases in NO_x production due to the exponential form of the rate constant of the first reaction in the extended Zeldovich mechanism.

Increasing x_b caused the trapped mixture to be more dilute, leading to a lower percentage of the trapped mass participating in combustion, which resulted in linear decreases in combustion temperatures. In the same manner and for the same reason as with TER, linear changes in combustion temperatures resulted in exponential changes in the

NO_x prediction. It was determined, however, that the NO_x prediction was much more sensitive to percentage changes in TER than to the same percentage changes in x_b because the combustion temperatures were more sensitive to percentage changes in TER.

The sensitivity analysis for SBT was an attempt to identify the fundamental thermodynamic reasons why increasing the intake air temperature causes such a dramatic increase in NO_x emissions. It was shown that as SBT increased, it resulted in linear increases in TER and T_{SOC}, and linear decreases in x_b. Based on the sensitivity analyses for TER and x_b, each of these factors would be expected to drive a direct, exponential relationship between SBT and NO_x, and such is indeed the case.

It was desired not only to identify the driving thermodynamic factors behind the NO_x versus SBT relationship, but also to quantify the relative importance of each factor. Based upon results presented in the previous two sensitivity analyses, it was argued that the adiabatic flame temperature could be seen as a representative, or characteristic, value for all of the combustion temperatures. Thus, any change in the adiabatic flame temperature could be seen as a change in the "combustion temperatures." Based upon this argument, it was shown that changing TER, T_{SOC}, and x_b accounted for 58%, 32%, and 9%, respectively, of the change in combustion temperatures with changing SBT.

Finally, the results from the three sensitivity analyses were examined in light of the presence of cycle-to-cycle variations in the experimental pressure data. It was shown that the average cycle behavior in terms of pressure is not necessarily the average cycle behavior in terms of NO_x production. Even very detailed multi-dimensional simulations would be susceptible to erroneous NO_x predictions if the simulation was validated for a

single, average pressure cycle. It was argued that since cyclic variability is a random phenomenon, and since NO_x can have such a sensitive, nonlinear relationship with the bulk thermodynamic properties in an engine, any one cycle should not be assumed to be representative of the average engine behavior in terms of NO_x production. Therefore, there is a need for future work in thermodynamic modeling that considers a range of actual cycles, coupled with a statistical model, to predict NO_x emissions with greater accuracy and reliability.

REFERENCES

[1] Energy Information Administration, "eia.gov," [Online]. Available: https://www.eia.gov/naturalgas/archive/analysis_publications/ngpipeline/index.html. [Accessed 4 February 2020].

[2] Innovative Environmental Solutions, Inc. & Optimized Technical Solutions, "Availability and Limitation of NOx Emission Control Resources for Natural Gas-Fired Reciprocating Engine Prime Movers Used in the Interstate Natural Gas Transmission Industry," The INGAA Foundation, Inc., 2014.

[3] Advanced Engine Technologies Corporation et al., "Pipeline Engine Emissions Control Roadmap," Pipeline Research Council International, Inc., 2005.

[4] Innovative Environmental Solutions, "Potential Impacts of the Ozone and Particulate Matter NAAQS on Retrofit NOx Control for Natural Gas Transmission and Storage Compressor Drivers," INGAA Foundation, 2018.

[5] J. McCarthy, "Air/GHG Regulations Impacting the Natural Gas Transmission Industry: 2018 Air Quality and GHG Regulatory Update," in *Gas Machinery Conference*, Kansas City, MO, 2018.

[6] C. D. Cooper and F. C. Alley, Air Pollution Control, Waveland Press, Inc., 2011.

[7] J. B. Heywood, Internal Combustion Engine Fundamentals, The McGraw-Hill Companies, Inc., 1988.

[8] J. B. Heywood and E. Sher, The Two-Stroke Cycle Engine: Its Development, Operation, and Design, Taylor & Francis, 1999.

[9] G. P. Blair, Design and Simulation of Two-Stroke Engines, Society of Automotive Engineers, Inc., 1996.

[10] T. F. Linker, *Predictive NOx Emissions Modeling for a Large Bore, Lean-Burn, Integral Compressor Engine,* Texas A&M University: M.S. Thesis, 2019.

[11] A. J. Haagen-Smit, "Chemistry and Physiology of Los Angeles Smog," *Industrial and Engineering Chemistry,* pp. 1342-1346, 1952.

[12] E. Robinson, Air Pollution: The Effects of Air Pollution, 2nd ed., vol. III, A. C. Stern, Ed., Academic Press, Inc., 1977.

[13] D. A. Vallero, Fundamentals of Air Pollution, 5th ed., Elsevier, Inc., 2014.

[14] Environmental Protection Agency (EPA), "Demonstrating Compliance with New Source Performance Standards and State Implementation Plans," [Online]. Available: https://www.epa.gov/compliance/demonstrating-compliance-new-source-performance-standards-and-state-implementation-plans. [Accessed 13 February 2020].

[15] D. Clerk, "The Theory of the Gas Engine," *Minutes of the Proceedings of the Institution of Civil Engineers,* 1882.

[16] J. A. Caton, An Introduction to Thermodynamic Cycle Simulations for Internal Combustion Engines, John Wiley & Sons, Ltd, 2016.

[17] D. J. Patterson and G. J. Van Wylen, "A Digital Computer Simulation for Spark-Ignited Engine Cycles," *SAE International,* 1963.

[18] K. J. McAulay, T. Wu, S. K. Chen, G. L. Borman, P. S. Myers and O. A. Uyehara, "Development and Evaluation of the Simulation of the Compression-Ignition Engine," *SAE Transactions,* vol. 74, pp. 560-593, 1966.

[19] J. A. Caton, "A Multiple-Zone Cycle Simulation for Spark-Ignition Engines: Thermodynamic Details," *ASME Internal Combustion Engine Division Fall Technical Conference,* 2001.

[20] C. Olikara and G. L. Borman, "A Computer Program for Calculating Properties of Equilibrium Combustion Products with Some Applications to I.C. Engines," *SAE International,* no. Technical Paper 750468, 1975.

[21] J. B. Heywood, J. M. Higgins, P. A. Watts and R. J. Tabaczynski, "Development and Use of a Cycle Simulation to Predict SI Engine Efficieny and NOx Emissions," *SAE Technical Paper Series,* 1979.

[22] D. E. Foster, "An Overview of Zero-Dimensional Thermodynamic Models for IC Engine Data Analysis," *SAE Transactions,* vol. 94, pp. 436-449, 1985.

[23] S. H. Mansouri, J. B. Heywood and K. Radhakrishnan, "Divided-Chamber Diesel Engine, Part I: A Cycle-Simulation which Predicts Performance and Emissions," *SAE Transactions,* vol. 91, pp. 1101-1132, 1982.

[24] Y. A. Cengel and M. A. Boles, Thermodynamics: An Engineering Approach, New York, NY: McGraw-Hill, 2008.

[25] C. R. Ferguson and A. T. Kirkpatrick, Internal Combustion Engines: Applied Thermosciences, 3rd ed., Wiley, 2016.

[26] L. Pauling, General Chemistry, New York: Dover Publications, Inc., 1988.

[27] G. P. Smith, D. M. Golden, M. Frenklach, N. W. Moriarty, B. Eiteneer, M. Goldenberg, C. T. Bowman, R. K. Hanson, S. Song, W. C. Gardiner, V. V. Lissianski and Z. Qin, "GRI-Mech 3.0," [Online]. Available: http://www.me.berkeley.edu/gri_mech/. [Accessed 14 May 2020].

[28] S. Gordon and B. J. McBride, "Computer Program for Calculation of Complex Equilibrium Compositions, Rocket Performance, Incident and Reflected Shocks, and Chapman-Jouguet Detonations," National Aeronautics and Space Administration, 1976.

[29] M. Rashidi, "Calculation of Equilibrium Composition in Combustion Products," *Applied Thermal Engineering,* 1998.

[30] NIST-JANAF, "NIST-JANAF Thermochemical Tables," [Online]. Available: https://janaf.nist.gov/. [Accessed 14 May 2020].

[31] G. Woschni, "A Universally Applicable Equation for the Instantaneous Heat Transfer Coefficient in the Internal Combustion Engine," *SAE International,* 1967.

[32] J. C. Wall, J. B. Heywood and W. A. Woods, "Parametric Studies of Performance and NOx Emissions of the Three-Valve Stratified," *SAE Transactions,* vol. 87, pp. 1469-1494, 1978.

[33] N. C. Blizard and J. C. Keck, "Experimental and Theoretical Investigation of Turbulent Burning Model for Internal," *SAE Transactions*, vol. 83, pp. 846-864, 1974.

[34] E. Sher, "Scavenging the Two-Stroke Engine," *Progress in Energy and Combustion Science*, vol. 16, no. 2, pp. 95-124, 1990.

[35] S. R. Turns, An Introduction to Combustion: Concepts and Applications, 2nd ed., McGraw-Hill, 2000.

[36] A. M. Dean and J. W. Bozzelli, "Combustion Chemistry of Nitrogen," in *Gas-Phase Combustion Chemistry*, Springer-Verlag, 2000, pp. 125-342.

[37] J. L. Brown, *Implementable Changes to a Large-Bore Single Cylinder Natural Gas Engine for Improved Emissions Performance*, Texas A&M University: M.S. Thesis, 2017.

[38] A. U. Bajwa, *First and Second Law Analyses of a Large Bore Two Stroke Spark Ignition Engine Fueled with Natural Gas*, Texas A&M: M.S. Thesis, 2016.

[39] Horiba, Ltd., *NO/NOx Analyzer CLA-720MA*, Kyoto, Japan, 2004.

APPENDIX A

CASES ANALYZED IN THE SENSITIVITY ANALYSIS

Table 4: Base Case

TER	x_b	SBT [K]	Exhaust [NO] [ppm]
0.7133	0.1488	314.5	174

Table 5: Sensitivity Analysis with Varying TER

Case	TER	x_b	SBT [K]	Exhaust [NO] [ppm]
+3% TER	0.7347	Base Case	Base Case	271
+6% TER	0.7561	Base Case	Base Case	410
+9% TER	0.7775	Base Case	Base Case	595
-3% TER	0.6919	Base Case	Base Case	108
-6% TER	0.6705	Base Case	Base Case	64
-9% TER	0.6491	Base Case	Base Case	37

Table 6: Sensitivity Analysis with Varying x_b

Case	TER	x_b	SBT [K]	Exhaust [NO] [ppm]
+3% x_b	Base Case	0.1532	Base Case	157
+6% x_b	Base Case	0.1577	Base Case	141
+9% x_b	Base Case	0.1622	Base Case	127
-3% x_b	Base Case	0.1443	Base Case	192
-6% x_b	Base Case	0.1398	Base Case	213
-9% x_b	Base Case	0.1354	Base Case	235

Table 7: Sensitivity Analysis with Varying SBT

Case	TER	x_b	SBT [K]	Exhaust [NO] [ppm]
+5 K SBT	0.7215	0.1475	319.5	226
+10 K SBT	0.7297	0.1463	324.5	291
+15 K SBT	0.7280	0.1450	329.5	370
-5 K SBT	0.7050	0.1500	309.5	132
-10 K SBT	0.6968	0.1513	304.5	100
-15 K SBT	0.6885	0.1525	299.5	75